FLEXIBLE GRAPHENE/CELLULOSE COMPOSITE FOR MULTIMODAL SENSING

OOI JING QUAN

UNIVERSITI TUNKU ABDUL RAHMAN

FLEXIBLE GRAPHENE/CELLULOSE COMPOSITE FOR MULTIMODAL SENSING

OOI JING QUAN

A project report submitted in partial fulfilment of the requirements for the award of Bachelor of Science Physics with Honours

Lee Kong Chian Faculty of Engineering and Science Universiti Tunku Abdul Rahman

May 2023

DECLARATION

I hereby declare that this project report is based on my original work except for citations and quotations which have been duly acknowledged. I also declare that it has not been previously and concurrently submitted for any other degree or award at UTAR or other institutions.

Signature :

Name : OOI JING QUAN

ID No. : 1901863

Date : 20/05/2023

APPROVAL FOR SUBMISSION

I certify that this project report entitled **"FLEXIBLE GRAPHENE/CELLULOSE COMPOSITE FOR MULTIMODAL SENSING"** was prepared by **OOI JING QUAN** has met the required standard for submission in partial fulfilment of the requirements for the award of Bachelor of Science Physcis with Honours at Universiti Tunku Abdul Rahman.

Approved by,

Signature   :

Supervisor   :   Dr. Tan Chun Hui

Date   :   20/05/2023

The copyright of this report belongs to the author under the terms of the copyright Act 1987 as qualified by Intellectual Property Policy of Universiti Tunku Abdul Rahman. Due acknowledgement shall always be made of the use of any material contained in, or derived from, this report.

ACKNOWLEDGEMENTS

I would like to express my sincere gratitude to all the individuals who have supported and inspired me throughout my journey in writing this thesis.

First and foremost, I would like to extend my heartfelt thanks to my supervisor, Dr. Tan Chun Hui, for his valuable time, guidance, comments, and suggestions, which have been instrumental in shaping this thesis. I would also like to acknowledge the support and encouragement of his postgraduate students, Thiresammy and Vinod Ganesan.

I would like to acknowledge the unwavering support of my family, who have been with me every step of the way in my undergraduate studies in Physics. Without their love and encouragement, I would not have been able to achieve this milestone.

Furthermore, I would like to express my appreciation to my internship company, whose fabrication and passivation work have inspired and motivated me to pursue my research in this field. I am truly grateful for the opportunity to work with such a dedicated and supportive team.

Lastly, I would like to thank all the individuals who have contributed to my growth and development throughout my academic journey. Your support, encouragement, and guidance have been invaluable to me, and I am deeply grateful for all that you have done. Thank you all.

ABSTRACT

Graphene's distinctive 2D lattice structure and electronic properties make it an ideal material for sensor applications, with flexibility, ultra-sensitivity, fast response time, and multi-sensing capabilities. However, pristine graphene is expensive and challenging to produce. As a result, attention has shifted to graphene derivatives and composites. Oxygenated graphene flakes are not only a cheaper alternative to pristine graphene but also introduce hydrophilic properties. Cellulose is a commonly used matrix material in nanocomposites that is non-toxic and effective in creating stable dispersion. In this project, we demonstrated solution approach to nano-engineer a non-toxic sensitive composite based on graphene nanoplatelets (GNPs) and hydroxyethyl cellulose (HEC) matrix. The sensing ink was brush-coated on paper substrate, and data acquisition was performed using an Arduino project to evaluate and quantify the sensing performance towards ammonia gas, temperature, bending, and human respiration. Passivation of the sensing layer enhanced the selectivity of targeted signal. The sensing ink demonstrated distinguishable signal response towards different stimuli indicating the feasibility to detect two signals simultaneously or development of integrated sensor. This low-cost and scalable sensing ink can bridge the gap between internet of things (IoT) and current sensor technology, which is mostly bulky, non-flexible, and single sensing. The composite has the potential to serve as electronic skin to aid human health or motion monitoring, environmental monitoring, and robotics applications.

TABLE OF CONTENTS

LIST OF TABLES

LIST OF FIGURES

LIST OF SYMBOLS / ABBREVIATIONS

S	Sensitivity
θ	Degree angle
E_a	Activation energy
K	Boltzmann constant
R_0	Baseline resistance, Ω
ΔR	Resistance change relative to baseline resistance, Ω
R_s	Sheet resistance, Ω/m^2
t	Thickness, m
V	Voltage, V
RET	Response time
REC	Recovery time
2D	two-dimensional
STD	Standard deviation
RMS	Root-mean-square
SNR	Signal-to-noise ratio
DI	Deionized
EC	Ethyl cellulose
HEC	Hydroxyethyl cellulose
rGO	Reduced graphene oxide
GO	Graphene oxide
GNP	Graphene nanoplatelet
SEM	Scanning electron microscope

LIST OF APPENDICES

CHAPTER 1

INTRODUCTION

1.1   Background

The growing demand for high-performance materials in various fields has led to the exploration of new and advanced materials. The pioneering achievement of graphene by Geim and Novoselov in 2009 defied doubts about the existence of low-dimensional materials and opened up vast promising applications Graphene is a 2D carbon allotrope. The unique lattice geometry and carbon-carbon strong covalent bonding give rise to novel mechanical, electronic, and thermal properties. Meanwhile, the high surface-to-volume ratio of graphene enables ultra-sensitivity, fast response time, and sensitive to various stimuli. These features make graphene a good sensing material.

Sensors are essential in today's world to monitor various environmental and biological parameters. The limitations of most current sensors are their bulkiness, rigidity, and single-sensing capabilities. In comparison, a graphene-based sensor provides lightweight, flexible, ultra-sensitive, fast response time, and multimodal sensing capabilities that can revolutionize traditional sensors into a wearable and highly compacted sensing layer that resembles electronic skin. The major challenges facing graphene products are manufacturing cost-effectiveness, process difficulty, and the tendency of graphene to agglomerate.

Thus, researchers have turned to the development of graphene derivatives. Graphene oxide (GO) is oxidized graphene that can occur naturally. GO, as an alternative to pristine graphene, mitigates the processing difficulty. Additionally, the oxygen functional groups in GO trade-off the higher electrical and mechanical properties for hydrophilicity, which is essential for moisture affinity and chemical reactivity for specific molecules such as ammonia. On the other hand, composite-making is a common technique used in nanotechnology by combining more than two materials to create a new material with tailored properties. A graphene composite consists of graphene nanoplatelets (GNPs) dispersed in a matrix material. The dispersion of nanoparticles is emphasized to prevent agglomeration. Many composite processing methods have been proposed to ensure cost-

effectiveness. One of the processing methods is colloidal processing, which is a low-temperature and straightforward solution approach.

Hydroxyethyl cellulose (HEC), a modified form of cellulose, is often chosen as the matrix material for biopolymer composites. HEC is a low-cost, abundant, and renewable material. Its current state-of-the-art application involves household and food products due to its non-toxicity, thickening, emulsifying, and stabilizing properties. These properties make HEC suitable for graphene composites as they allow for effective and stable dispersion of graphene nanoplatelets (GNPs) to form GNP networks. The water-soluble nature of HEC gives water-retaining properties that increase the structural integrity of graphene sheets, preventing aggregation or collapse. The non-ionic nature of HEC avoids interaction with graphene and preserves the attractive properties for sensing. Consequently, the GNP networks in the HEC matrix unify nanoscale graphene to compensate for good flexibility and self-adhesion between graphene layers, enhancing the mechanical properties of the graphene composite and making it a robust flex sensor. Additionally, a graphene/cellulose composite combines the high thermal stability of HEC and the high thermal conductivity of GNPs, making it advantageous for temperature sensing. Moreover, HEC is biocompatible, making graphene composite attractive for wearable electronic sensors. In conjunction with sustainable technology development, the GNP/HEC composite is a biodegradable material.

1.2   Motivation of the Study

Sensors are essential tools for a wide range of applications, including healthcare, machinery and environmental monitoring. With the rise of the Internet of Things (IoT), there is an increasing demand for devices that can provide real-time monitoring for smart applications or system management. However, most current sensors suffer from several limitations, including bulkiness, rigidity, and single-sensing capabilities. These limitations make it challenging to integrate sensors into wearable devices and other flexible systems. Moreover, single-sensing devices can only detect one signal, limiting their ability to provide comprehensive information about the environment or the human body.

To address these limitations, the development of flexible, robust, and sensitive sensing materials is of great importance. One promising material for this purpose is a graphene/cellulose composite. This composite material combines the outstanding sensing properties of graphene with the non-ionic nature, biodegradability, high thermal stability, thickening, and water-retaining capabilities of cellulose. The resulting material can be tailored to specific applications and can detect multiple signals through multimodal sensing.

Several research studies have investigated the use of graphene/cellulose composites for sensing applications, but more research is needed to explore their full potential. Specifically, the design of a flexible and versatile composite material that can be integrated into electronic skin for multimodal sensing is still a challenge. Therefore, the proposed study aims to fill this gap by developing a flexible graphene/cellulose composite for multimodal sensing and exploring its potential applications in electronic skin.

By addressing the limitations of current sensors and offering a versatile and multimodal sensing material, the proposed study has the potential to revolutionize the field of sensing, comparable to the invention of the touchscreen. Essentially, electronic skins enable the development of innovative applications in healthcare, environmental monitoring, and human-machine interfaces.

1.3   Problem Statement

The aim of this study is to revolutionize the current sensor technology by developing a flexible and multimodal sensing layer that can replace the existing bulky, rigid, and single-sensing sensors. Graphene-based sensors, such as graphene field-effect transistor (FET) sensors, have demonstrated superior performance in terms of sensitivity, response time, miniaturization, and flexibility compared to traditional sensors. However, the high cost associated with the direct growth of high-quality graphene (e.g., CVD) has hindered their commercialization. As a result, researchers have turned their attention to graphene derivatives (e.g., GO, rGO, GNPs, and laser-induced graphene (LIG)) for sensor applications. Specifically, the composites of graphene nanofillers with a biocompatible cellulose matrix for sensing applications are limited addressed.

In this project, the main research problem is the development of a low-cost manufacturing process that can produce a flexible graphene/cellulose composite for multimodal sensing. To address this problem, a low-temperature composite-making method and scalable delivery techniques will be explored. The sensing performance of the graphene/cellulose composite will be evaluated using four different sensing modals: mechanical testing with bending angles, thermal testing with temperature variations, chemical reaction testing with exposure to ammonia gas, and complex stimuli testing with human respiration. The results of these tests will showcase the versatility of the sensing layer and its potential applications in healthcare and environmental monitoring.

Additionally, several research questions will need to be answered to guide the resolution of the main research problem. Firstly, the study will identify the synthesis and fabrication recipe of the graphene/cellulose composite for a flexible sensing layer. Secondly, the sensing mechanism of the composite material will be reviewed. Thirdly, an experiment will be designed to evaluate the performance of various sensing modal of the composite material. Lastly, the composite's sensing performance will compare to traditional sensors and existing works on graphene-based sensors.

Overall, this study aims to establish a foundation of understanding for graphene composite electronic skin, which can be utilized to enhance future prototypes and achieve the ultimate goal of developing a low-cost, practical, and effective electronic skin.

1.4   Aim and Objectives

The main objective of this project is to demonstrate graphene/cellulose composite for flexible and multimodal sensing utilizing open-source easy-to-use microcontroller modules as data logger. The followings are the breakdown of the main objectives:

(1)   To identify the characteristics of the graphene/cellulose composite as flexible multimodal sensing materials

(2)   To evaluate the sensing mechanism and performance of fabricated devices with different architectures in multimodal sensing.

1.5　　Scope and Limitations of the Study

The scope of the project is to develop a flexible graphene/cellulose composite for multimodal sensing. The project aims to use graphene as the sensing material and cellulose as the polymer matrix. To ensure the feasibility of the project, the composite making will use a low-temperature synthesis method, and a scalable delivery technique will be prioritized for the fabrication of a flexible sensing layer. The proposed sensing layer will require hardware and software assistance to acquire and analyze signal data. Specifically, the hardware assistance will be provided by the Arduino UNO R3, while the software assistance will be provided by the Arduino IDE and OriginLab 2019b.

　　　　The prototype will be capable of detecting multiple types of stimuli, including ammonia gas, temperature, bending, and human respiration. The functionality and sensing performance of the prototype towards targeted signals will be quantified, while minimizing conflict with other signals. However, there are some limitations to the project, including the selection of material fabrication methods, the optimization of the composite material, the ability to measure multiple stimuli simultaneously, and the reliability and reproducibility of the prototype's sensing performance.

CHAPTER 2

LITERATURE REVIEW

2.1   Introduction

This chapter reviews the use of graphene/cellulose composite materials for flexible and resistive-based multimodal sensing layers. The chapter begins with an introduction to graphene and cellulose, including their derivatives, production methods, properties, and roles in the sensing mechanism. Subsequently, existing works related to this topic are reviewed, covering topics such as the synthesis and fabrication of graphene/cellulose composites, their sensing mechanisms, and their performance in various sensing applications. Finally, the importance of flexible and multifunctional sensors is discussed, highlighting the potential of this technology to address current limitations in the sensing market.

2.2   Properties of Materials

2.2.1   Graphene

The Roadmap of Graphene" by Novoselov et al. (2012) provides a comprehensive overview of graphene, from the realization of the first two-dimensional material to its properties, applications, and challenges in production. In definition, the term "graphene" broadly refers to single-layer and multi-layer up to ten layers, while pristine graphene commonly refers to material with low defects, low impurities, and a flat monolayer structure. The first isolation of graphene from highly oriented pyrolytic graphite was achieved using the mechanical exfoliation method by Geim and Novoselov in 2004, and the research group characterized the graphene. The measurements showed good agreement with the theoretical predictions of its novel properties.

A pure monolayer graphene is made up of carbon in a single atomic-thick layer with a honeycomb lattice structure, as shown in Figure 2.1(a). A carbon atom has four valence electrons, and in the graphene structure, each carbon atom is sp^2-hybridized and forms three σ-bonds (also known as strong covalent bonds) with the three nearest-neighbour atoms in a trigonal planar geometry (Yang et al., 2018). As a result of interatomic bonding, monolayer

graphene has excellent mechanical properties, characterized by a high tensile strength (130.5 GPa) and a Young's modulus (1 TPa) (Lee et al., 2008). Because of the strong covalent bonding and tightly packed atoms in the high-ordered graphene crystal, the thermal conductivity is remarkable. A high-quality suspended single-layer graphene has been shown to have a thermal conductivity of 3000-5300 W/mK (Balandin, 2011; Balandin et al., 2008), compared to copper's 400 W/mK. Moreover, the high surface area-to-volume ratio is likely to allow more surface atoms to participate in thermal vibration, and the 2D structure limits phonon scattering. As graphene's thermal conductivity is dominated by phonon mode, its thermal conductivity is highly influenced by lattice defects, impurities, interfacial interactions, and the number of layers (Pop et al., 2012; Yan et al., 2015). Nevertheless, the strong covalent bonding of graphene ensures good resistance to thermal degradation. With respect to the tightly packed atomic structure and strong carbon-carbon bonds of pristine graphene, it has excellent impermeability to all gas and liquid (Bunch, 2008).

Continuing on the graphene bonding by Yang et al. (2018), the remaining unhybridized p-orbital of a carbon atom forms a π-bond that is perpendicular to the planar structure as shown in Figure 2.1(e). The π-bond among neighbouring atoms overlap to form a delocalized and conjugated π-electron system across the 2D geometry. The periodic potential of the π-electron system across the homogenous atomic composition give rise to the Dirac cone features at the K- and K'-point in the electronic band structure as shown in Figure 2.1(b), Figure 2.1(c) and Figure 2.1(d).
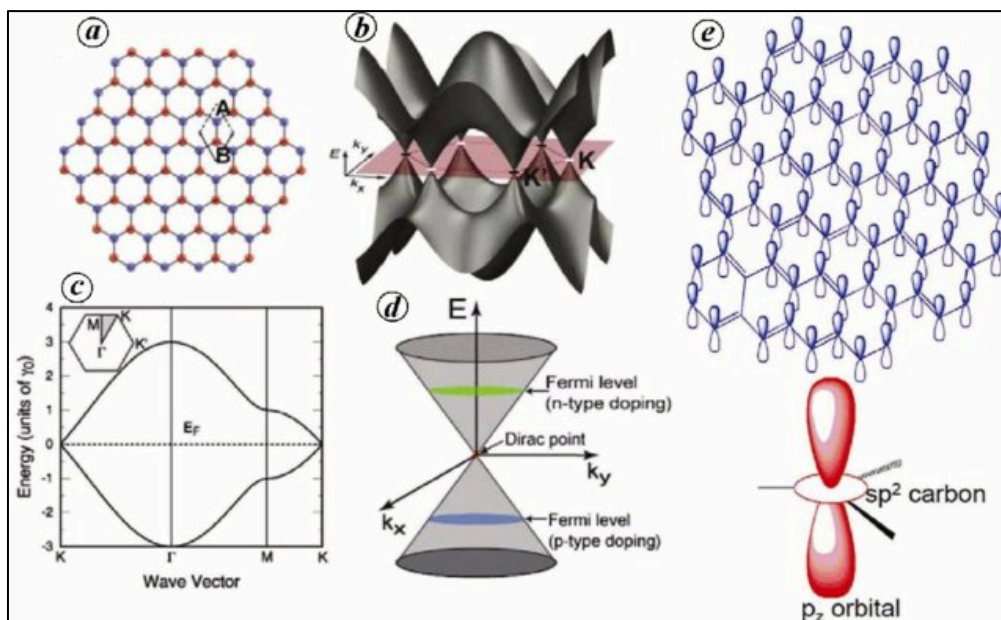
Figure 2.1: (a) Two carbon atoms (A and B) per unit cell in the hexagonal lattice structure of graphene; (b) Three-dimensional band structure of graphene; (c) Energy-momentum in *k*-space diagram of graphene; (d) Dirac cone diagram with low-energy level at Dirac point and Fermi-level position varied with doping; (e) Schematic of the graphene sp^2-hybridization for sigma bonds and delocalized conjugated p_z-orbitals (Ojha et al., 2014).

The Dirac cone in the graphene band structure has two unique characteristics: zero bandgap and a linear dispersion relationship. This is in contrast to most semiconductor materials, which exhibit a sizable bandgap and a parabolic relationship. Firstly, the zero bandgap implies that valence electrons can be easily excited to the conduction band and move freely to conduct electricity. Secondly, the density of states at the Dirac point is intrinsically high. Thirdly, the curvature of the band structure is inversely proportional to the effective mass, and graphene has zero effective mass electrons, leading to high electron mobility ($\sim 2 \times 10^5$ cm$^2 \cdot$V$^{-1} \cdot$s^{-1}) and ballistic transport (Mayorov et al., 2011). Therefore, the unique electronic band structure allows graphene to have outstanding electrical conductivity ($\sim 10^6$ to 10^8 S$\cdot$cm^{-1}) depending on the growth method and process (Cao et al., 2015). Additionally, high conductivity in a high-quality crystal lattice is inherent with low electrical noise. As a

semiconductor, graphene exhibits a resistance-temperature relation that can be expressed as (Shahil and Balandin, 2012)

$$R \propto R_0 e^{(-E_a/2KT)} \qquad (2.1)$$

where

R = measured resistance, Ω

T = temperature detected by the sensor, K

R_0 = resistance at a finite temperature, Ω

K = Boltzmann constant, 8.6173×10^{-5} meV/K

E_a = thermal activation energy, meV

Apart from the intrinsic novel properties of graphene, the application of asymmetrical strain and bending can disturb the electron density and change the electronic properties. According to Levy et al. (2010), elastic strain changes in graphene result in a rare phenomenon known as strain-induced pseudo magnetic field. In simple words, an asymmetrical strain in a graphene sheet can cause the charge carriers to circulate the strain field, similar to the effect of a uniformly applied magnetic field perpendicular to the graphene layer, resulting in the formation of a nanobubble. The pseudo magnetic field is of incredible magnitude, exceeding that of any actual magnetic field. In an experiment, a 0.5 nm tall and 4 nm wide nanobubble induced 100 T of pseudo magnetic fields. Irani et al. (2022) have reinforced that isotropic strain increases electron scattering and decreases resistance, while no bandgap opening exists. In contrast, asymmetrical strain induces a pseudo-magnetic field, resulting in an open band gap. Bending can be considered a form of asymmetric strain on graphene, as it involves stretching on one side and compressing on the other side parallel to graphene. Studies show that the bandgap opening for asymmetric strain is applied parallel and perpendicular to the graphene sheet. For example, multilayer graphene on a polymethyl methacrylate (PMMA) substrate was measured with a gauge factor of 50, making it an excellent piezoresistivity for strain and bending detection. Bandgap opening not only increases the electronic resistance but also increases

light absorption. Combining the exceptional strength and flexibility of graphene and the pseudo magnetic field effect, strain engineering on the nanoscale can manipulate the electronic structure without the need for an electric field for bandgap opening.

On the other hand, the π-electron system contributes to van der Waals forces, which are generally attractive to atoms or molecules in solid, liquid, or gas states (Bunch, 2008). Thus, weak van der Waals interactions between graphene and other chemicals or materials can disturb the electron density, resulting in different electronic properties, which serve as sensing capabilities. Similarly, interlayer interactions in multilayer graphene modify the electronic structure and deviate from the linear dispersion relationship observed in monolayer graphene. Van der Waals interactions in multilayer graphene allow the possibility of electrons to travel across the layers, resulting in additional bands and bandgap opening, as shown in Figure 2.2. Combining its large surface area-to-volume ratio and nanoscale conductive network, graphene is capable of fast response sensing and rapid recovery.
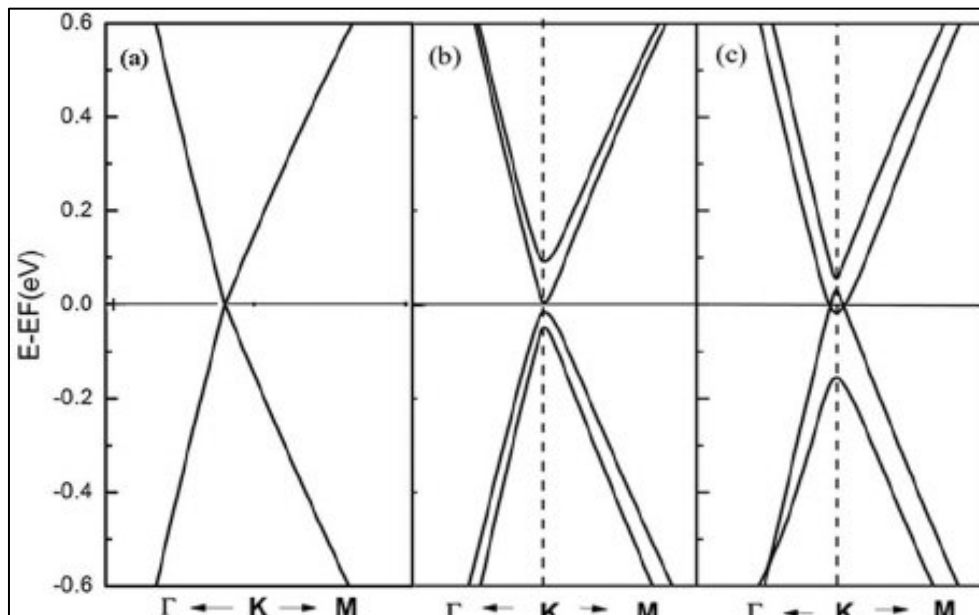
Figure 2.2: The band structures of (a) single-layer graphene; (b) bilayer graphene where AB atoms stacking; (c) bilayer graphene stacking on hexagonal boron nitride (Li et al., 2012b).

Given the many novel properties of graphene, it has gained increasing interest for use in the fields of sensors (Nag et al., 2018), transistors (Kim et al., 2010), solar cells (Yin et al., 2014), and energy storage (Li et al., 2012a; Pech et al., 2010). Despite its feasibility, mass production of graphene for industrial scale applications should be low-cost, scalable, reproducible, and of suitable quality. The existing mature production technologies (e.g., epitaxial growth and chemical vapor deposition) face challenges in terms of efficiency, scalability, and cost-effectiveness (Zhong et al., 2015). The authors suggested three alternative routes for graphene production using graphite flakes, which are low-cost and naturally abundant. In overview, the liquid-phase exfoliation route is extremely simple and cost-effective in producing conductive graphene suitable for flexible graphene-based sensors with amenability to specialized sensing modes. The dispersion of graphite flakes in low boiling solvents (e.g., deionized water) can be aided by mechanical stirring. However, pristine graphene tends to agglomerate shortly due to interplanar interaction. Thus, the authors proposed surfactant-assisted liquid-phase exfoliation, followed by the potential delivery methods of graphene nanocomposite sensing ink, such as inkjet printing and doctor-blading methods.

2.2.2   Oxygen-Functionalized Graphene Nanoplatelets

The low dispersibility of pristine graphene can be overcome by replacing it with graphene oxide. Generally, graphite tends to oxidize naturally to graphite oxide, where various hydrophilic functional groups are added. Alternatively, artificial oxidative treatment of graphite such as the modified Hummer's method (Zhang and Yang, 2017) effectively increases oxygen concentration and enhances uniform oxidation. Oxidization of graphene introduces hydroxyl and epoxy to the basal plane as well as carboxyl and carbonyl to the edges, as illustrated in Figure 2.3(a).
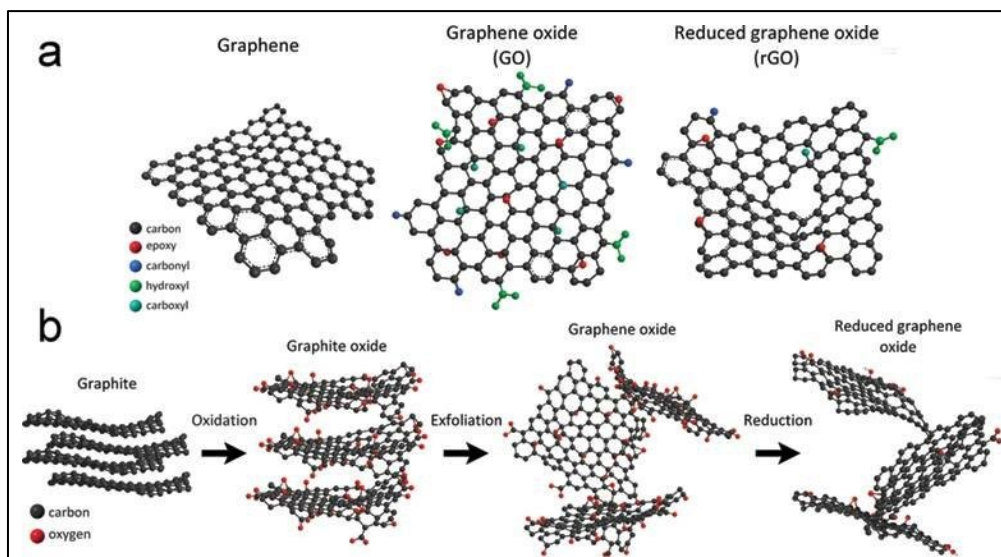
Figure 2.3: (a) Chemical composition and lattice structures of Graphene, GO, and rGO; (b) The production sequence of exfoliated GO and rGO from Graphite. (Raval, 2018).

Primarily, oxidation of graphite makes it hydrophilic due to the presence of oxygen functional groups. Essentially, the oxidation process weakens the van der Waals interactions and interlayer coupling (Dong et al., 2017). Additionally, the varying height of functional groups is also a factor that eases the exfoliation process. However, graphene oxide trades off the unique electron band structure of pristine graphene, as illustrated in Figure 2.4. According to Fuji and Enoki (2013), the hydroxyl and epoxy groups remove a π-electron, whereas carbonyl groups add a π-electron. This disruption of the π-electron network of graphene and breaking the symmetry of local sublattice results in bandgap opening and reduced conductivity. Fundamentally, the oxygen-containing functional groups attached to graphene can change the intrinsic sp^2-hybridization to sp^3-hybridization (Yao et al., 2012). On the other hand, the presence of oxygen groups in graphene makes it hydrophilic, which can be advantageous for water purification using graphene oxide membranes (Han et al., 2013).
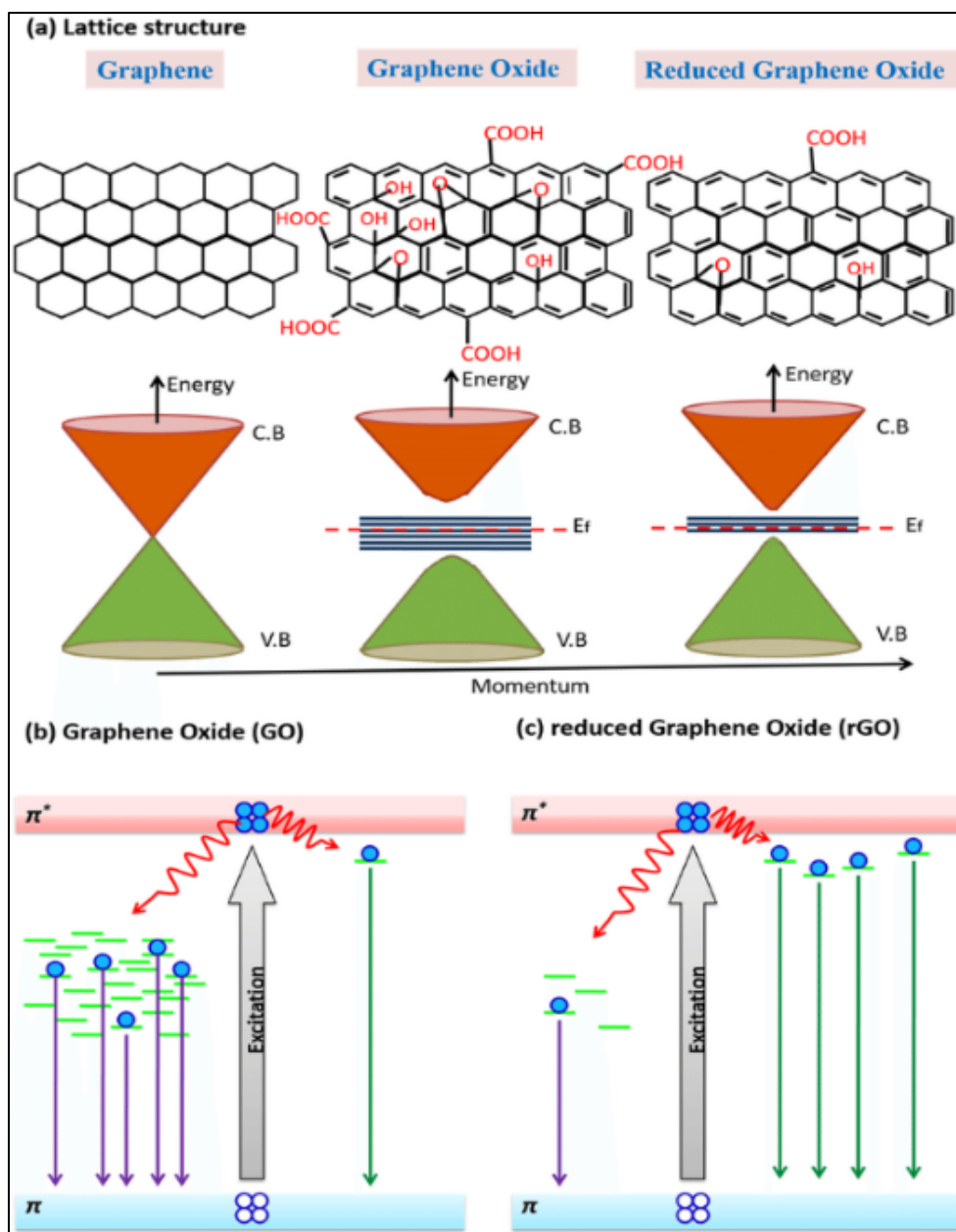
Figure 2.4: (a) Lattice structure and band diagram of graphene, graphene oxide, and reduced graphene oxide, respectively; (b) Electronic transitions in graphene oxide, and (c) electronic transitions in reduced graphene oxide (Abid et al., 2018).

Oxygenated graphene has able to detect humidity with low intrinsic noise due to the crystal lattice quality and high electrical conductivity (Lv et al., 2019). The resistivity of graphene increases with increasing humidity due to the adsorbed water molecules, which results in proton-electron exchange and changes the bandgap of the material (Naik and Krishnaswamy, 2016; Quellmalz et al., 2018). The relative dielectric permittivity of graphene oxide

(GO) also increases with the water uptake (Huang et al., 2018). The responsiveness of graphene to its surrounding conditions has proven to have both positive and negative effects on graphene-based sensor. This is because changes in humidity levels in the environment can cause alterations in the graphene carrier concentration and mobility. (Melios et al., 2018). The adsorption of water molecules at grain boundary defects in graphene can lead to an increase, decrease, or non-monotonic behaviour of resistance with changes in film structure (Popov et al., 2017). In summary, the resistance of graphene decreases with an increased relative humidity level due to the adsorption of water molecules on the graphene surface, which changes the bandgap of graphene and increases its relative dielectric permittivity.

As a supplement, liquid-phase exfoliated graphene oxide can undergo reduction to partially recover the outstanding properties of pure graphene as illustrated in Figure 2.3(b). Spyrou and Rudolf (2014) discussed several reduction processes, such as thermal annealing, chemical reduction, electrochemical reduction, and photochemical reduction. It is worth noting that the oxidation-reduction production of graphene results in less purity compared to direct production methods from high-quality graphite. Theoretical findings and experiments agree that reducing the oxygen ratio in graphene oxide from 75.00 % to 6.25 % is manageable.

In short, replacing pristine graphene with graphene oxide flakes as the starting material in the dispersion can efficiently mitigate agglomeration issues. Additionally, reduction of exfoliated graphene oxide is recommended to improve the quality of the sensing ink.

2.2.3 Cellulose

Cellulose is one of the most abundant biopolymers that are commonly found in the cell walls of plants. The monomers of cellulose biopolymer are β-D glucose molecules which are made up of a six-carbon ring with five hydroxyl groups and a single aldehyde group. The glucose monomers assemble into a long linear chain through the hydroxyl groups forming β (1-4) glycosidic bonds with two adjacent glucose units as illustrated in Figure 2.5.
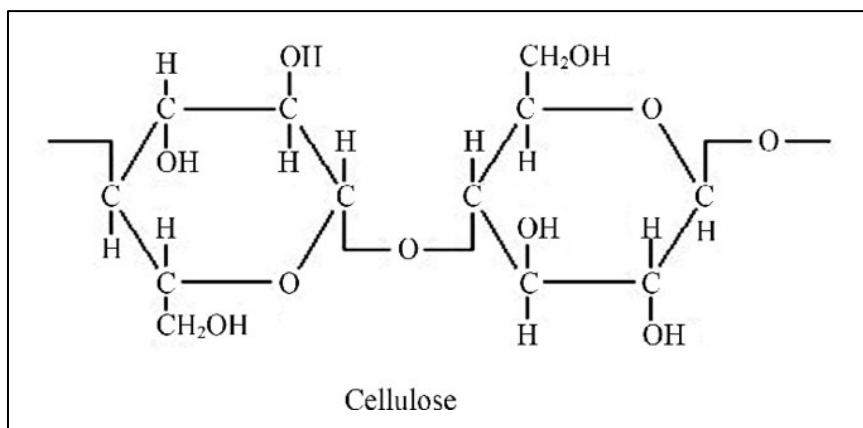
Figure 2.5: Structure formula of cellulose (Richards, Baker and Iwuoha, 2012).

The repeating glucose monomers range from 10,000 to 15,000 units per molecule (Habibi, 2014). The long linear chain is known as cellulose microfibril, while a strand of cellulose microfibril bound together via hydrogen bonds forms a cellulose polymer (Nishiyama et al., 2003). The inherent properties and strong interfacial bonding between cellulose fibres and polymer matrix lead to proven mechanical properties (e.g., elastic modulus of 138 GPa, Young's modulus of 128 GPa, and tensile strength of 17.8 GPa) and thermal properties (Nishino, Matsuda and Hirao, 2004). Research findings have shown that all-cellulose composites possess a near-zero thermal expansion coefficient (10^{-7} K^{-1}), while the cellulose matrix displays good linear thermal expansion behaviour ($1.4 \times 10^{-5} \text{ K}^{-1}$). Both non-linearity and high linearity of thermal expansion are preferred for graphene-based sensing ink. Nonetheless, cellulose is insoluble in water, which limits its profit value in sensing applications in aqueous environments (El Fawal et al., 2018).

The production of cellulose begins with extraction from plant sources, such as wood and cotton, followed by a series of mechanical, chemical, and enzymatic treatments that vary with the type of plant material and desired purity of the end product. Briefly, the plant material is cleaned of dirt and debris, followed by chopping and pulping to break down the cell walls, and finally bleaching to isolate the cellulose from other components (Zhang, Y.H.P and Lynd, 2004). The production of cellulose is complex but yields a high volume of low-cost product; the annual production amount is estimated at 10^{11} tons (Klemm et al., 2005).

The historical uses of cellulose involve the production of paper and textiles. Recently, cellulose composites have been investigated for advanced material applications in packaging, automotive, and construction due to their unique properties. Moreover, the biodegradability and low toxicity of cellulose nanoparticles have made them versatile in biomedical applications (Seddiqi, 2021).

Overall, cellulose is an abundant and low-cost material that is environmentally friendly, low-toxicity, and possesses excellent mechanical and thermal properties. Moreover, cellulose is available in fibre or matrix form for use in composites.

2.2.4   Cellulose Esters

Hydroxyethyl cellulose (HEC) and ethyl cellulose (EC) are derivatives of cellulose esters and non-ionic in nature. Figure 2.6 shown the structure of basic HEC, some of the hydrogen atoms in the three reactive hydroxyl groups in a cellulose molecule is substituted by hydroxyethyl group (CH_2CH_2OH).
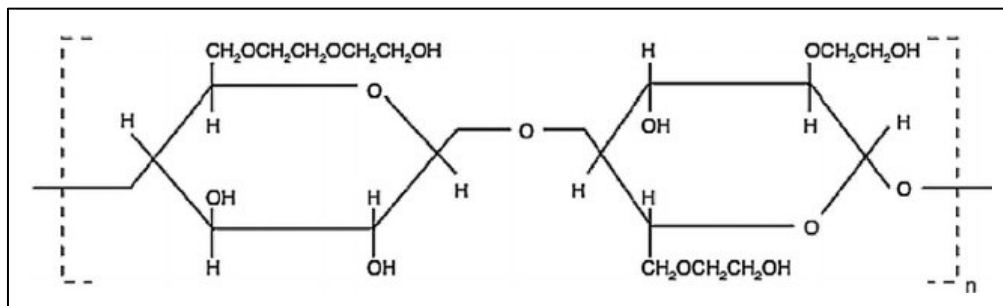
Figure 2.6: Structural formula of hydroxyethyl cellulose (Zulkifli et al., 2014).

The hydroxyethyl groups are the key to solubility in polar solvent (e.g., water) due to the high affinity for polar molecules and hydrogen bonds formation (Noreen et al., 2020). Whereas Figure 2.7 shown the structure of EC, some of the hydroxyl groups in cellulose molecule are replaced by ethyl groups. The degree of substitution determines the solubility (Davidovich-Pinhas, Barbut and Marangoni, 2015).
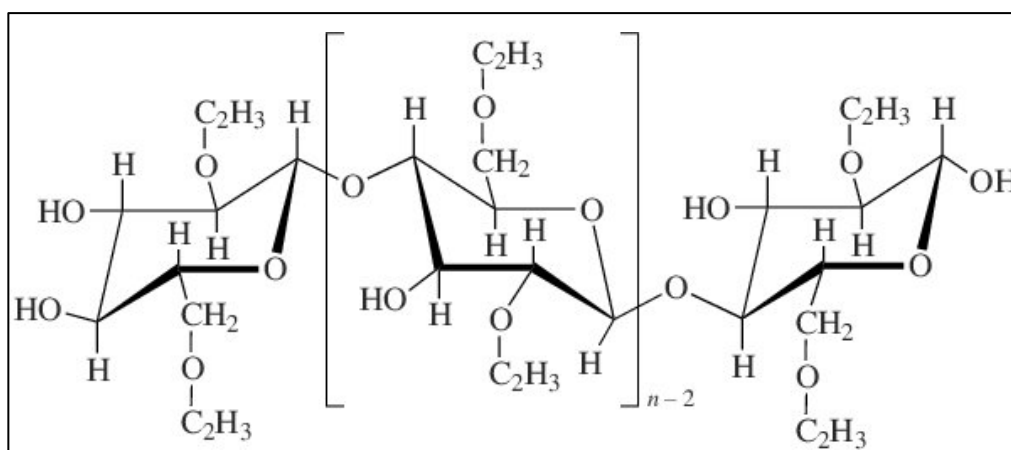
Figure 2.7: Structural formula of ethyl cellulose (Myasoedova and Shchegolikhin, 2008).

Typically, EC is insoluble in polar solvents; however, it is soluble in organic solvents. The polarity of the ethyl group is different from the polarized oxygen in water molecules. Thus, no hydrogen bonding occurs between EC and water, resulting in its hydrophobic nature.

HEC has proven to have thickening and dispersion properties and can be used as a matrix. The hydroxyl groups on the HEC backbone form hydrogen bonds with water molecules, resulting in a water-retaining three-dimensional network structure that thickens the viscosity of the solution. The degree of substitution and weightage of HEC are factors affecting the viscosity of the solution (Benyounes, Remli and Benmounah, 2018). Additionally, the viscosity of the HEC matrix can be affected by increasing temperature as the hydrogen bonds between HEC molecules weaken. However, the effect is reversible before it is heated at a high temperature (~ 100 ℃) for too long (Blažková, Hrivikova and Lapčík, 1990). While HEC can interact with the polar groups of the particle surface, reducing the interparticle attraction, it is able to prevent particle agglomeration and form stable dispersion. On the other hand, EC can form intermolecular hydrogen bonding through the ester linkages on the backbone, forming a gel-like structure and thickening the solvent. Due to its high molecular weight and branched structure, EC shows a good thickening effect even at a low concentration. In addition to the branched structure of EC, it is able to trap particles in the solvent and create stable dispersion. An extra feature of EC is its emulsifying properties due to its

amphiphilic nature. A stable emulsion can be formed with the participation of EC, where the hydrophobic ethyl groups attract the non-polar phase, and the hydrophilic cellulose backbone attracts the polar phase.

HEC is produced through the reaction of cellulose with ethylene oxide in an alkaline medium and a catalyst (Abdel-Halim, 2014). In contrast, EC is produced through the reaction of cellulose with ethyl chloride catalysed by zinc chloride. The degree of substitution of hydroxyethyl groups is determined by the process temperature, reaction time, and reactant concentration. HEC and EC are commercially available in powder, flake, or pellet forms. Furthermore, due to their biocompatibility and non-toxicity, they have been widely used in various applications. For example, HEC is used as a thickener and stabilizer in the food, cosmetic, and pharmaceutical industries (Benyounes, Remli and Benmounah, 2018). Meanwhile, EC is commonly used as a binder and coating agent for tablets and capsules in the pharmaceutical industry (Wasilewska and Winnicka, 2019). Recently, HEC has been researched as a matrix material for drug delivery systems (Ho et al., 2022), and EC has been studied for the development of new composite materials (Ouarga, 2020).

In short, the thickening and dispersion properties of HEC and EC depend on their concentration, degree of substitution, and temperature. They are both biodegradable and biocompatible and are commonly used in coating and film formation. However, HEC is water-soluble which can enable humidity detection for sensing ink, whereas EC is water-insoluble which may limit its applications in aqueous environments. Nevertheless, it can be used to passivate sensing ink from moisture.

2.3   Review of Related Existing Works

Several papers have been published demonstrating the manufacturing of flexible graphene-based sensors with multimodal sensing through a low-cost and simple process of solution approach. Liu et al. (2019a) reported the fabrication of an aqueous carbon black (CB) and reduced graphene oxide (rGO) on a cellulose paper substrate. The dispersion was sprayed onto a patterned plastic sticker masked on printing paper to form the sensitive electrode and connected by copper wires. The authors emphasized that aqueous rGO can form a uniform sensing layer, while CB particles can cause cracking of the

sensing layer. CB particles are equivalent to agglomerations of graphene nanoplatelets (GNPs). Therefore, exfoliation, dispersing, and stabilization treatments of GNPs must be emphasized. Additionally, the authors suggested the use of a polymer matrix to thicken the dispersion and reduce the need for multiple rounds of spraying-drying method in electrode coating. The flexible CB/rGO sensing layer exhibited varying resistance with bending, humidity, temperature, and pressure. Ghosh et al. (2014) reported that rGO-coated filter paper exhibited a resistance response to ammonia with good selectivity.

For the sensing mechanism of graphene/polymer composites to ammonia, Hizam, Al-Dhahebi and Mohamed Saheed (2022) explained that the interaction of ammonia molecules with graphene/polymer composites can occur at three different locations: [1] oxygenated groups on graphene material, [2] the interface between the graphene layers and nano-polymer, and [3] intercalation between the graphene layers. Seekaew et al. (2014) explained three possible sensing mechanisms of graphene composite-based sensors toward ammonia molecules. Firstly, the direct charge transfer process occurs from electron-donating ammonia molecules to the holes in p-type graphene, thus increasing the sensing element resistance. Secondly, the reduction process occurs between ammonia and chemisorbed oxygen (from the environment) on the p-type graphene surface, transferring electrons to the conductive film, thus increasing the resistance. Thirdly, the diffusion of ammonia molecules into the polymer matrix can expand the interchain spacing and disrupt the conductive pathways of the graphene-polymer network, thus increasing the resistance. Subsequently, the ammonia-induced resistance effect on graphene composites can be reversible as the ammonium reacts with oxygen in the air and desorbs.

Continuing with the synthesis of graphene/cellulose composite, Zhang and Yang (2017) documented the component ratio and process of manufacturing a GO/HEC composite to form a thin film via the solution mixing-evaporation method. Ultrasonication was used to disperse the GO in the HEC matrix. The findings showed that the hydrogen bonding by the polymer matrix improved the thermal stability of the oxygenated group in GO. Additionally, increased GO content decreased the composite's oxygen permeability of the sensing layer. Meanwhile, Mardi, Risi Ambrogioni and Reale (2020) documented the synthesis and fabrication method of a GNP/EC

composite. Terpineol and acetic acid were added to the composite to reduce naturally oxidized GNPs and chemically exfoliate GNPs, respectively. A combination of ultrasonication and ball milling was used to ensure the homogeneity of GNPs dispersion. The composite was used to form a thin film via the blade-coating method. The findings showed thermoelectric behaviour and Ohmic behaviour of the composite thin film, which agreed with findings by Sadasivuni et al. (2015). The authors highlighted that the GNPs ratio above the ratio was crucial to the material conductivity due to the overlapping GNPs network structure.

Essentially, the coating technique of solution-approached composites provides a cheaper route compared to chemical vapor deposition (CVD). In addition to the above-mentioned delivery techniques, Yoshida et al. (2022) suggested screen-printing, and Qi et al. (2020) reported that Meyer-rod coating could achieve a thin electrode layer. Dang Luong et al. (2011) demonstrated a smooth and fracture-free layer of graphene/cellulose composite coated via vacuum filtration, but the process is relatively long. Nonetheless, a graphene paper produced via vacuum filtration displays better electrical and sensing responses towards humidity and mechanical strain compared to dip-coated graphene paper (Khalifa et al., 2020). Many studies have used paper as the flexible substrate due to its low cost, and the paper pores have been reported to tightly hold the sensing ink. Meanwhile, Fu et al. (2021) proposed that the HEC matrix is versatile enough to wet other more durable flexible substrates such as cotton fabric and PET film. Liu et al. (2018) introduced the use of plasma etching to create micro-pores on a flexible substrate to promote the wettability of the sensing ink.

To summarize, the graphene/cellulose-based composite sensing ink can be synthesized easily via solution approach at low temperature. Graphene flakes can be mechanically exfoliated and dispersed using ultrasonication and/or ball milling. The cellulose polymer matrix is able to stabilize and thicken the graphene dispersion. The composite has been reported to respond to multiple stimuli and can wet various flexible substrates. Several delivery techniques for the composite sensing ink, such as screen-printing, blade-coating, and rod-coating, pose low process difficulty and duration, enabling scalability.

2.4 Significance of Flexible Multimodal Sensors

The Internet of Things (IoT) enables a seamless communication and connectivity between various devices and systems. Sensors play a critical role in the IoT ecosystem, providing data on the physical world for monitoring and driving decision-making and automation. However, the limitations of current sensor technology, such as bulkiness, rigidity, and limited sensing capabilities, have posed challenges in achieving the full potential of IoT applications (Anwer et al., 2022). In contrast, graphene/cellulose self-sensing nanocomposites have the potential for flexibility and multimodal sensing, making them the next-generation sensor technology, similar to electronic skin.

Flexibility is a key requirement for sensors in the IoT era. Traditional sensors are typically bulk and rigid, limiting their application in certain scenarios where flexibility is crucial, such as wearable devices for environment, machine or healthcare monitoring (Trung and Lee, 2016). To illustrate, rigid sensors may not conform to curved surfaces or may be uncomfortable to wear on the human body, hindering their usability in wearable devices. Flexible sensors, on the other hand, can conform to curved surfaces, stretch and bend without losing functionality, and can be integrated seamlessly into various form factors (Khan et al., 2016). Meanwhile, flexible sensors are typically manufactured from nano-scaled printed sensing layers, giving them additional features such as lightweight and ultra-sensitivity. Recently, human e-skins or smart bandages have gained attention in biomedical technology due to their ability to detect vital signs such as heart rate, pulse, near-surface blood flow, metabolites on the skin and saliva, and throat vibration, among many others, for health and fitness monitoring, diagnosis, and therapeutic purposes (Vilela, Romeo and Sánchez, 2016). Additionally, a machinery e-skin based on stretchable strain sensors has been developed for the exterior of aircraft for structural health monitoring and introducing 'fly by feel', enhancing human-machine interaction (Yin et al., 2017). The ultra-thin and flexible sensors that are wearable on machinery improve robustness and reduce the risk of the sensor device from heavy friction, rotation, and vibration in machinery movement. The flexibility feature is desired in a wide range of IoT applications, including smart wearables and

industrial automation, where the ability to adapt to different shapes and sizes is critical.

Multimodal sensing is essential for unlocking the full potential of IoT applications. Current sensors often specialize in a single type of sensing, such as temperature, pressure, or motion, limiting their versatility and adaptability. For example, a traditional humidity sensor may not be able to provide additional contextual information, such as temperature or chemical composition, which may be relevant in certain IoT use cases. In contrast, multimodal sensors have the ability to simultaneously measure multiple parameters, enabling more comprehensive and context-aware data collection. The graphene-composite based multi-sensing sensor not only monitors moisture in human skin or rhythm and depth of breath, but also detects the contents of ions in sweat or traces of ammonia in exhaled air. These are critical indicators of personal health and fitness applicable in physiological health tracking and sports performance (Liang et al., 2020). Similarly, multi-sensing sensors can detect and monitor changes in pressure, vibration, and temperature, which are significant for tactile sensing in robotics (Haroun et al., 2021). Utilizing multi-sensing sensors in a system can enhance its dependability and resilience, expand the system's ability to observe time and space, advance the precision and credibility of information, and diminish the system's investment in redundancy (Segev-Bar et al., 2017)

The flexible and multimodal sensing sensors will bridge the gap between current sensor technology and the requirements of the IoT. Flexible sensors can be seamlessly integrated into a wide range of objects and surfaces, enabling new applications that were not previously feasible. Multimodal sensing allows for more comprehensive and contextual data collection, leading to improved decision-making, automation, and overall system performance in the IoT ecosystem. Apart from their technical advantages, graphene/cellulose composite-based flexible and multimodal sensors also have potential for commercialization, making them more accessible and affordable for widespread adoption in IoT applications. Moreover, the ability of multimodal sensors to provide multiple functionalities in a single device reduces the need for multiple sensors, simplifying the system design, reducing costs, and improving energy efficiency.

CHAPTER 3

METHODOLOGY AND WORK PLAN

3.1 Introduction

This chapter explains the experimental design of the prototype in parallel with the project objectives. Meanwhile, the availability of resources (e.g., chemicals, materials, software, hardware) and cost estimation were outlined to ensure the practicality of the project. Therefore, a project work plan incorporating the scope, availability, and cost was scheduled for the given timeframe of six months. The final methodology for the fabrication, material characterization, and performance evaluation of the prototype was recorded.

3.2 Experimental Design

The literature reviews indicated the multi-sensing capabilities of graphene, hydroxyethyl cellulose (HEC) as a dispersive and thickening agent with hydrophilic properties, and the flexible sensitive composite is expected to fill the gap of the sensors and IoT. The prototype composite was postulated to have a flexible and conductive network of graphene sheets that can give rise to sensing capabilities toward ammonia gas, bending, temperature, and human respiration.

The experiment began with the synthesis of the GNP/HEC composite. Additional reducing agent (e.g., terpineol) and chemical exfoliating agent (e.g., acetic acid) were not considered in this study to avoid the influence of external agents to the properties of GNP/HEC. Within the project scope, the synthesis recipes were not aimed for optimization; however, they were quickly determined by systematic adjustments referencing secondary research findings. The composite was verified with visual quality inspection for its dispersion, viscosity, and texture.

In the second work stage, the fabricated composite was coated on the paper substrate and sent for characterization in terms of physical, chemical, and electrical properties, reflecting the quality of the materials used, solution approach process and delivery method.

In the third work stage, four sensing layers were fabricated and customized to enhance selectivity of the targeted signal through passivation against other undesired signals. The designated sensing layers were tested for performance against targeted stimuli at varying stimulus intensity. Since the raw signal behaviour of the prototype, including internal noise and environmental noise (e.g., temperature fluctuation and air current), was the project focus, the signal conditioning circuits were not considered. Two stratifications in the project, such as the characterization and sensing performance evaluation of the prototype, were expected to be conducted within two weeks since preparation to prevent serious degradation deviating the sensing performance. Each set of performance testing was conducted in the same conditions to reduce the possibilities of errors, as no calibration guidelines of the first prototype.

3.3 Project Planning and Management

After understanding the experiment design, the project work stages can be arranged in a sequential flow as shown in Figure 3.1.
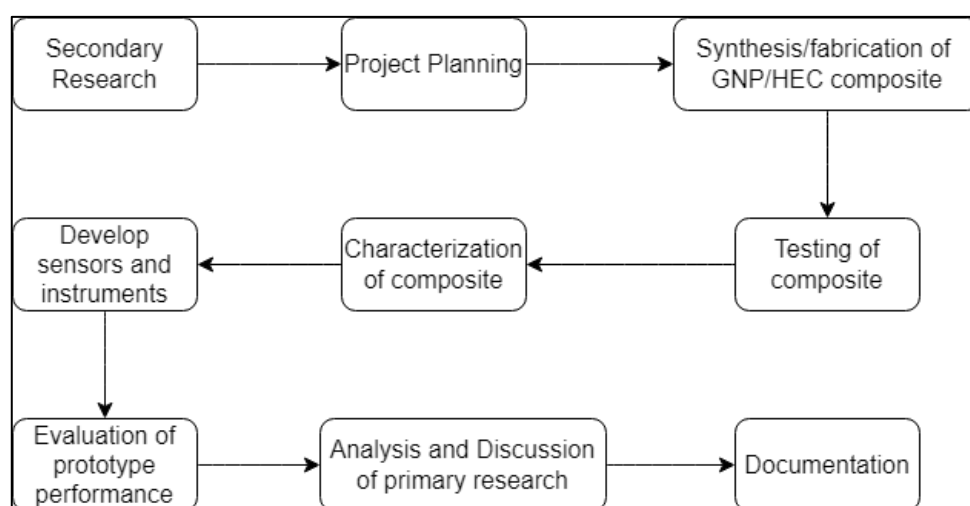
Figure 3.1: Project work stages in sequential flow.

3.3.1 Resource Allocation

Graphene nanoplatelets (GNPs; 5 μm particle size, nominal surface area 120 - 150 m^2/g; Sigma-Aldrich, USA), 2-hydroxyethyl cellulose powder (HEC; Mv 1300,000; Sigma-Aldrich, USA), ethyl cellulose powder (EC; 48 % ethoxy;

Sigma-Aldrich, USA), and ethanol (90 %). Deionized water (DI water; treated with Mili-Q integral water purification system, 12 M$\Omega \cdot$ cm). Ammonium hydroxide solution (NH$_4$OH; 28.0 - 30.0 % NH$_3$; Sigma-Aldrich, USA). Filter paper (raw material, high-quality cotton; pore size 20 - 25 μm; diameter 15 cm)

The laboratory equipment required for the synthesis and fabrication process were magnetic stirrer hot plate (0 - 1500 rpm; highest temperature 500 °C), magnetic stirrer bars (20 mm × 7 mm), glass bottles (20 ml), ultrasonic cleaner (model WUC-A03H; 40kHz; Daihan Scientific, Korea), electronic weighting scale. Electronic cutting machine (Silhouette Portrait, Austria). Polyimide tape (thickness 0.055 mm; width 10.000 mm; temperature resistance -73 to 300 °C; dielectric strength 7,000 V). PET sticker sheet (waterproof; thickness 0.05 - 0.08 mm).

The facilities that were accessible and necessary for material characterization were: EDX/SEM (EDAX-AMETEK, USA) and four-point probe (Ossila Instrument, UK) which required to book before use.

Testing instruments or concepts for prototype sensing performance: hot plate (Temperature-sensing); manual operating three-point bend testing (Bending test); An existing self-assembled plastic container using gas pump for venting and using Arduino Mega as data acquisition (ammonia gas sensing test), mouth breathing (Humidity test); Arduino UNO R3, open-source Arduino IDE, and voltage divider circuit (Data acquisition).

3.3.2   Cost Estimation

As the project emphasizes synthesizing a low-cost graphene/cellulose composite with flexible and multimodal sensing capabilities, thus this section provides the estimated cost of the raw materials of the prototype sensing layer (shown in Table 3.1).

Table 3.1   Cost of raw materials (Source from Sigma-Aldrich.com).

Raw materials	Estimated cost
GNPs	RM 44,880/kg
2-HEC	RM 833.00/kg

3.3.3   Schedule

The project constitutes two phases with total 14 weeks per phase. The project schedule is constructed using Gantt chart to arrange the time frame for each task defined in the work stages in one-piece flow, as shown in Figure 3.2 and Figure 3.3.

Tasks	Gantt Chart (Phase 1)													
	June 2022		July 2022					Aug 2022				Sep 2022		
	17/6	24/6	1/7	8/7	15/7	22/7	29/7	5/8	12/8	19/8	26/8	2/9	9/9	16/9
Literature Review	▓	▓	▓	▓										
Resources Allocation		▓	▓	▓										
Identify synthesis recipe of GNP/HEC composite					▓	▓	▓							
Identify synthesis recipe of EC solution					▓	▓	▓							
Testing of synthesized materials					▓	▓	▓							
Material Characterization of Fabricated GNP/HEC								▓	▓	▓	▓			
Develop data acquisition									▓	▓	▓			
Documentation							▓	▓	▓	▓	▓	▓	▓	▓

Figure 3.2: Gantt chart for phase-one schedule of the project.

Tasks	Gantt Chart - Phase 2													
	Feb 2023				March 2023					April 2023				May 2023
	3/2	10/2	17/2	24/2	3/3	10/3	17/3	24/3	31/3	7/4	14/4	21/4	28/4	5/5
Reproduce GNP/HEC composite	▓			▓			▓			▓				
Develop sensor prototype for targeted sensing mode	▓			▓			▓			▓				
Ammonia gas detection test	▓	▓												
Temperature-sensing test			▓	▓										
Bending detection test						▓	▓							
Humidity test									▓	▓				
Data analysis and Documentation					▓	▓	▓	▓	▓	▓	▓	▓	▓	▓

Figure 3.3: Gantt chart for phase-two schedule of the project.

Scheduling is a crucial component in project management prior to execution. Milestones are set and used as a measure of project progress to ensure the project can be completed on time. The first phase of the project involves laboratory access and the preparation of materials/chemicals. Secondary research can be conducted in parallel with resource allocation. Subsequently, the appropriate functional composite must be identified as a prerequisite for material characterization to reduce the number of scheduling of facilities that consume time for non-value-added waiting procedures. Data acquisition was given the lowest priority in phase one, which focused on synthesis and material characterization.

In the second phase of the project, the synthesis and fabrication process can be quickly done by reproducing the findings from phase one. Synthesis and prototype device customization to sensing performance testing must be conducted within two weeks to prevent potential degradation of sensing properties. Four sets of synthesis to prototype customization and testing were prescribed corresponding to four target stimuli. Ammonia gas detection and temperature sensing were given higher priority due to the demand for laboratory facilities. In comparison, bending detection and humidity testing were not constrained to laboratory facilities and required less testing duration, and could be worked on in parallel with data analysis and documentation.

3.4   Experimental Procedure

Figure 3.4(a) shows the procedure of synthesis of GNP/HEC composite as sensing ink. GNP powder (0.25 g) and deionized water were mixed in a 20 ml bottle followed by ultrasonic bath at room temperature for 30 minutes. HEC (0.30 g) was added into the GNP dispersion with mechanical stirring with magnetic stirrer at 1500 rpm, 50 °C for 60 minutes to produce a composite of HEC and GNPs. The synthesized composite was visual inspected for its quality such as white precipitation (undissolved HEC particulates) or dark blobs (undispersed GNPs); viscosity and texture by observation a drip of composite on a filter paper.

Figure 3.4(b) shows the fabrication of GNP/HEC sensing ink as flexible sensor for targeted signal. Filter paper was covered by a transparent vinyl paper with designed pattern (7.0 cm × 1.0 cm) using electronic cutting

machine. The GNP/HEC composite was brush coated uniformly on the paper and the excess composite is removed by using doctor blade method. The sensitive composite coated substrate is dried on a hot plate at 50 °C. The conductive layer is verified using a multi-meter. The sensitive layer was cut-out followed by a pair of tin coated copper strips attached at the two ends of the conductive layer. Pure GNP/HEC sensor prototypes were used for ammonia gas detection and humidity detection. For bending detection mode, a bare GNP/HEC sensor was well laminated with polyimide tape at the sensing face and backside. For temperature-sensing mode, a pure GNP/HEC sensor was brushed coated with EC/Ethanol mixture. The preparation of EC/Ethanol mixture as such: EC (0.4 g; Sigma-Aldrich, USA) was added into the 10 ml ethanol with mechanical stirring with magnetic stirrer at 500 rpm, 50 °C for 45 minutes to produce a matrix of EC. In short, four sensor prototypes were designed and developed for ammonia gas, temperature, bending, and respiration monitoring test, respectively (refer to Appendix A)
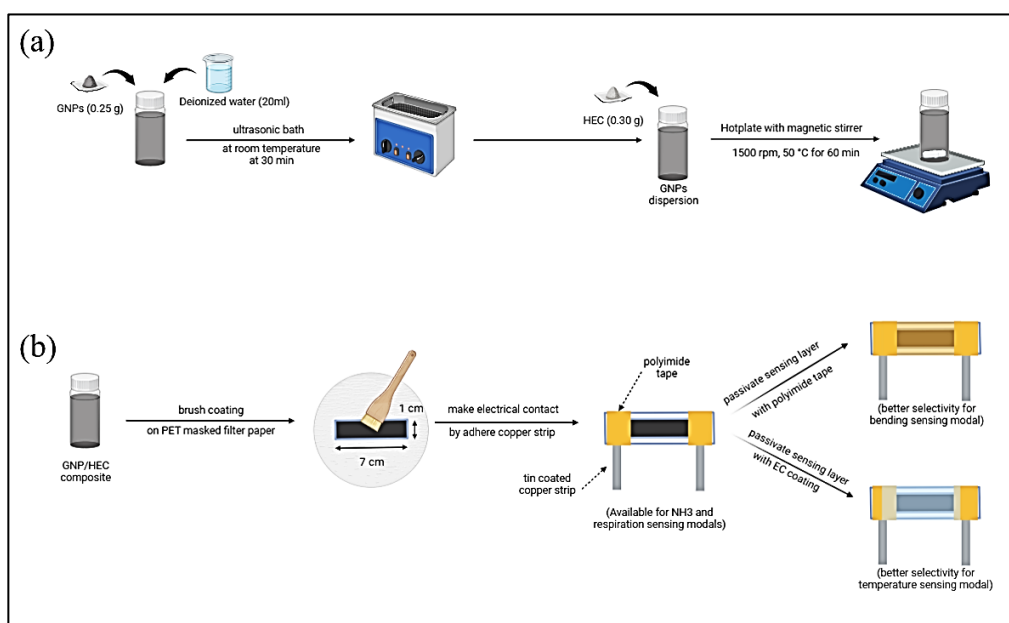
Figure 3.4: Schematic representations of (a) GNP/HEC composite synthesizing procedures and (b) prototypes fabricating and customizing procedures (Created with Biorender.com).

3.4.1 Characterization of GNP/HEC Composite

The paper-based sensitive layer was visualized by SEM at the surface morphology and cross-sectional analysis. The sheet resistance was examined using four-point probe. The characterization was conducted with random sampling and evaluation for average results.

3.4.2 Construction of Data Acquisition using Arduino project

A sensor prototype was connected to an Arduino voltage divider circuit (shown in Figure 3.5) with a suitable fixed resistance ~ 100,000 Ohm, such that the output at ambient is around the half of 1023 bit value. The microcontroller analogue read the sensory resistance, and the data showed the voltage signal in 10-bit. Additionally, the Arduino programmed to convert the sensory output bit-value to resistance value (refer to Appendix A).
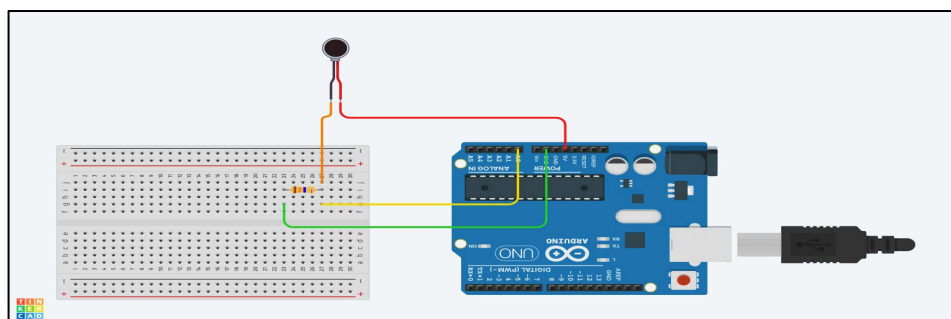
Figure 3.5: Configuration of Arduino UNO R3 voltage divider project for data acquisition (Created with Thinkercad.com).

3.4.3 Evaluation of the Prototype Sensing Performance

For ammonia gas sensing, the sensing layer (7.0 cm × 1.0 cm) was cut into a small piece (4.0 cm × 1.0 cm) and connected to data acquisition in the gas chamber (refer to Appendix A). The sensing layer is initialized for 10 minutes, and ammonia solution is dripped into the gas chamber to create a 15, 45, 75, 120, 150 ppm in the chamber for ammonia gas exposure for 15 minutes, followed by ammonia gas removal for 15 minutes. For bending detection, the prototype was supported onto a flexible plastic support to perform three-point bend testing (refer to Appendix A) which initialized at flat geometry (0°) to different angles (Compression: -80°, -70°, -60°, -50°, -40°, -30°, -20°, -10°; Expansion: +10°, +20°, +40° and +60°) and relaxed. For temperature-sensing,

the prototype was initialized at room temperature and exposed to constant temperature at 38 °C, 51 °C, 64 °C, 77 °C and 90 °C using a hotplate until the signal reached stagnant the prototype is removed from the hotplate for cooling. For respiration monitoring test, the prototype was lied in flat geometry and exposed to exhalated air.

The ammonia gas concentration is created from evaporation of ammonia water in the closed container. The relation between volume of ammonia water and maximum concentration in the container can be calculated using the relation

$$Cppm = \frac{V_{NH_4OH} \times D_{NH_3} \times W}{M_{NH_3} \times V_c} \qquad (3.1)$$

where

C_{ppm} = concentration of ammonia in the container, ppm

V_{NH4OH} = volume of ammonia water dispensed in the container

D_{NH3} = density of ammonia molecule, given 0.73 kg/m^3

W = weightage of ammonia in ammonia water, given 30 %

M_{NH3} = molecular mass of ammonia, given 17.031 g/mol

V_c = volume of the container, given 2 L.

Thus, the concentration of ammonia gas according to the volume of ammonia water can be calculated as recorded in Table 3.2.

Table 3.2: Conversion of volume of ammonia water dispensed in the container to the maximum concentration of ammonia gas.

Volume of NH₄OH (µl)	Concentration of ammonia gas (ppm)
100	15
300	45
500	75
800	120
1000	150

The measurement of angle in the three-point bend testing is illustrated in Figure 3.6. The local point at the middle of the sensing layer. The bending angle is measured from the lowest point to the highest point. The bending angle is negative equivalent to compression state (GNP/HEC composite layer on concave side) where the sensing layer is bent inward. Vice versa, the bending angle is positive equivalent to expansion state (GNP/HEC composite layer on convex side) where the sensing layer is bent outward.
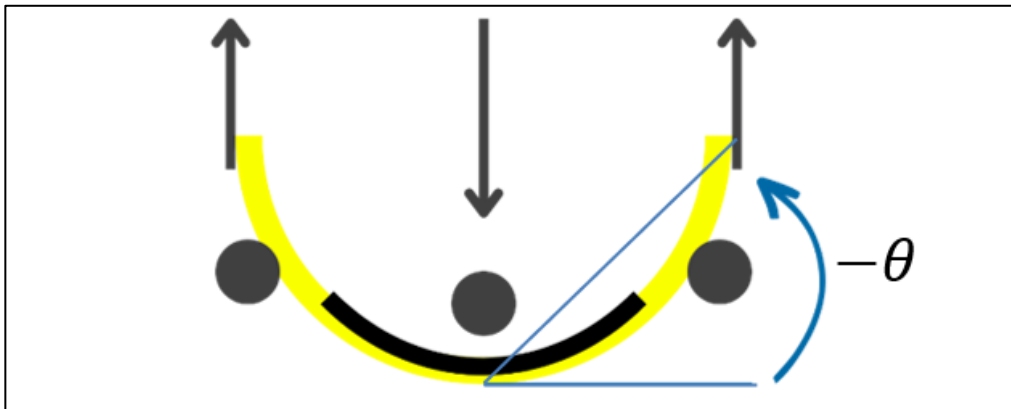

Figure 3.6: Mechanism of three-point bend test to prototype and measurement of bending angle (Created with Canva).

CHAPTER 4

RESULTS AND DISCUSSION

4.1 Introduction

The goal of this project was to develop a commercially viable electronic skin, by demonstrating the potential of using a graphene/cellulose composite for flexible and multimodal sensing, utilizing readily available and user-friendly microcontroller module, Arduino UNO R3, and a voltage divider circuit as a data acquisition. In this chapter, we present and discuss the material characteristics of the sensing layer, followed by the sensing performance of the prototype, discussing both dynamic and static sensing conditions. The experimental data presented in this chapter have been slightly smoothed to facilitate estimating the response time (RET) and recovery time (RCT). We have curve-fitted the signal response to analyse the relationship between the signal and the intensity/presence of the stimulus. The sensing performance results are related to the sensing mechanism and compared with existing sensors or results from related works.

4.2 Material Characterization of GNP/HEC Composite

The material characteristics of the 2-HEC/GNP composite, synthesized via colloidal processing and brush coating methods, are confirmed using SEM/EDX and 4-point probe. Figure 4.1 shows a magnified SEM image of the morphology, which exhibits crumpled graphene nanoplatelets tightly stacked on the 2-HEC fibres, indicating strong interfacial adhesion between surfaces. The size of the exfoliated graphene was measured between 7.940 to 21.519 μm. The overlapping of the graphene nanoplatelets in varying sizes, derived from ultrasonic treatment, allows for modulation of the connection and disconnection state between the graphene nanoplatelets in stretching and compressing, as used in bending (Liu et al., 2019b). The reduced SEM image on the sensing layer (shown in Figure 4.2) inspects the compact surface of graphene-coated 2-HEC fibres on the paper substrate, constructing a thick network structure of conductive graphene layers, supported by Mardi, Risi Ambrogioni and Reale (2020).
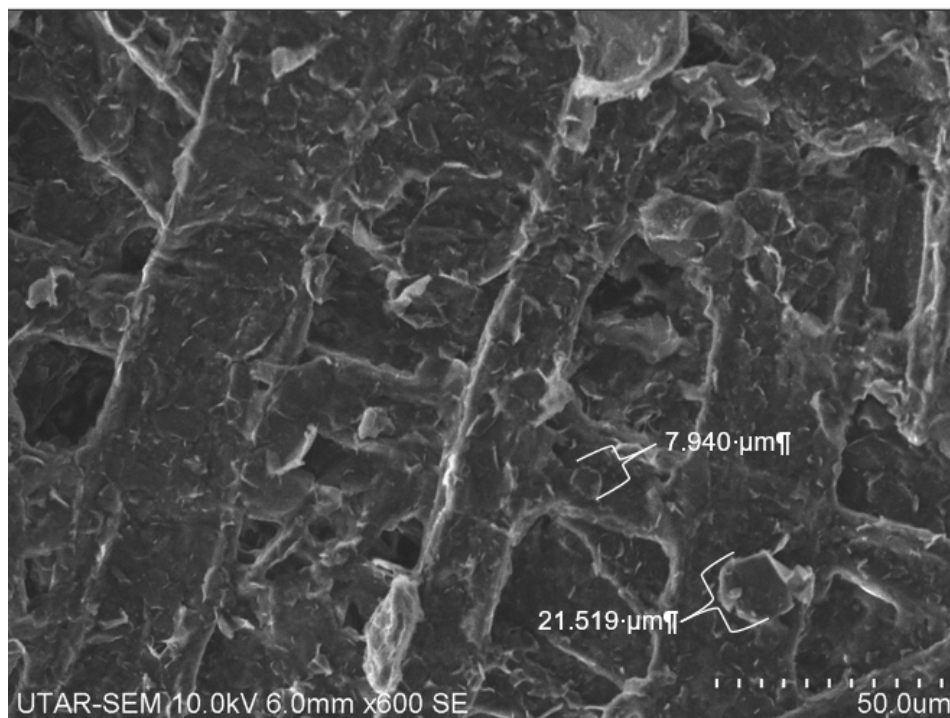
Figure 4.1: SEM image of GNPs on sensing layer with labelling of the size of
the graphene flakes (Obtained from UTAR-SEM).
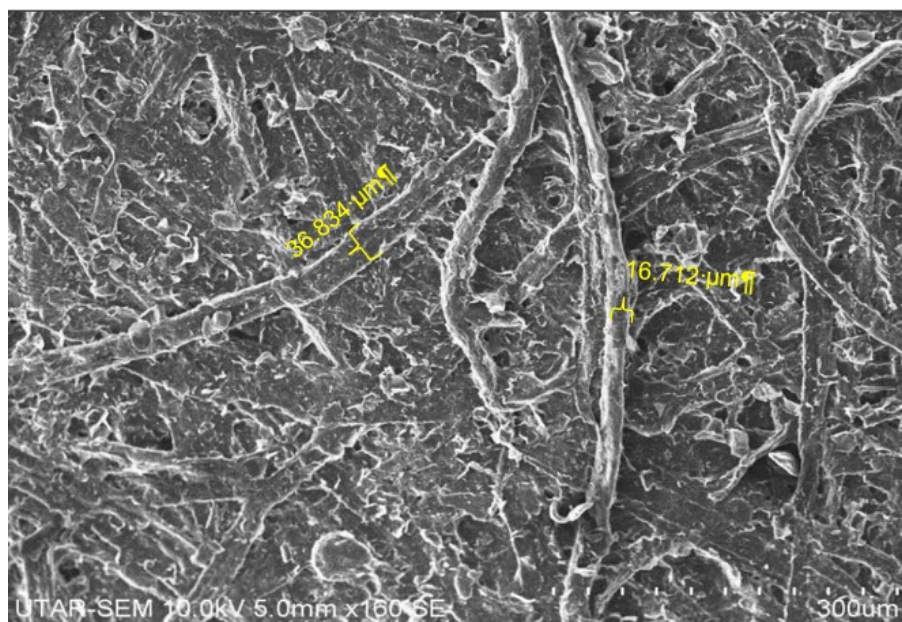
Figure 4.2: SEM image of HEC fibres with labelling of the size of the fibres
(Obtained from UTAR-SEM).

A homogeneous distribution of carbon and oxygen with no
substantial impurities is observed, confirming that the ink's conductivity is

dominated by the graphene flakes and oxygen defects (refer to Figure 4.3(a)). Furthermore, the EDX microanalysis report shown in Figure 4.3(b) reveals a high atomic percentage ratio of oxygen to carbon (0.47:1) in the composite, confirming that the graphene nanoplatelets were naturally oxidized and had not been reduced.
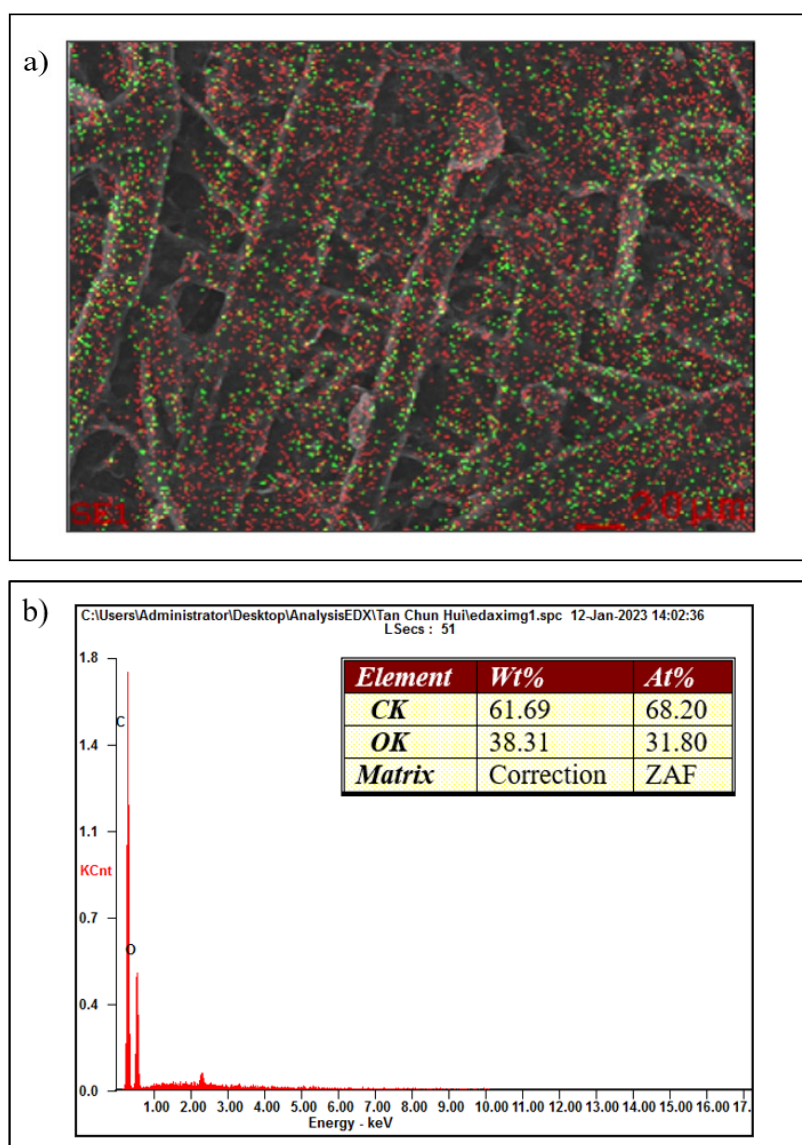
Figure 4.3: EDAX microanalysis report of a SEM image of GNP/HEC composite: (a) (red) carbon and (green) oxygen distribution mapping, and (b) Percentage of carbon and oxygen.

The cross-section of the brush-coated GNP/HEC composite on paper substrate is visualized by SEM and measured by ImageJ using the scale, as illustrated in Figure 4.4. The GNP/HEC composite layer and cellulose paper substrate are

distinguishable by the orientation of the fibrous layer due to the coating direction. The deposited composite is stacked on the paper substrate following the paper's grainy texture surface to improve the adhesion and sensitivity for bending sensing. A small gap between the composite and paper substrate is noticed, indicating a slight loss of adhesion between surfaces. The average thickness is estimated to be 24.799 μm over a sample of 50 data randomly collected from 10 SEM images. The sample thickness shows a standard deviation of 6.536 μm induced by the grainy texture of the cellulose filter paper. The thickness distribution of the brush-coated composite layer is close to a normal distribution, suggesting good confidence in overall thickness variation. In comparison to Qi et al. (2020), whose Meyer-rod coating method of graphene solution on mulberry paper produced a single-layer graphene at 13.1 μm with uniform deposition and no visible gaps between the surfaces.
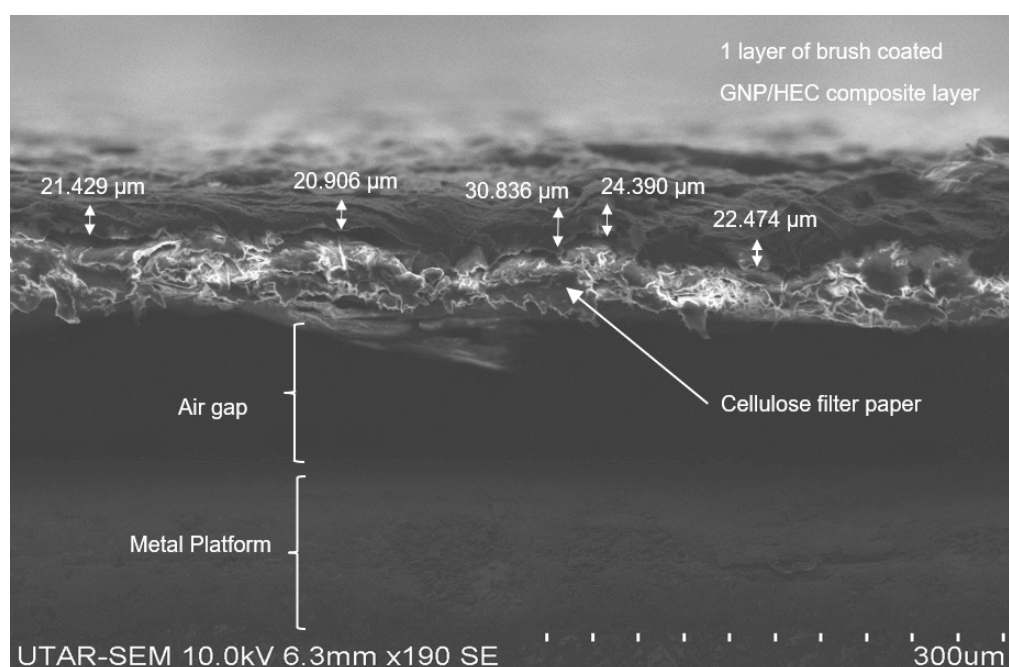
Figure 4.4: Example of SEM cross-sectional image of GNP/HEC sensing layer with thickness variation at five different locations (Obtained from UTAR-SEM).

Apart from the microscopic view, the GNP/HEC composite showed no sedimentation after 14 days compared to the just-prepared sample, indicating that the synthesis process was not well-formulated for creating good dispersion

of component materials (as shown in Figures 4.5(a) and 4.5(c)). Subsequently, the composite ink appeared homogeneous, dark-coloured, and had a thick texture with no extra diffusion of solvent in the surrounding area of the filter paper, thus supporting the thickening and stabilizing of the HEC matrix (as shown in Figure 4.5(b)). The average conductivity of the sensing layer characterized at 8.16398 S·m^{-1} can be found in Appendix B.
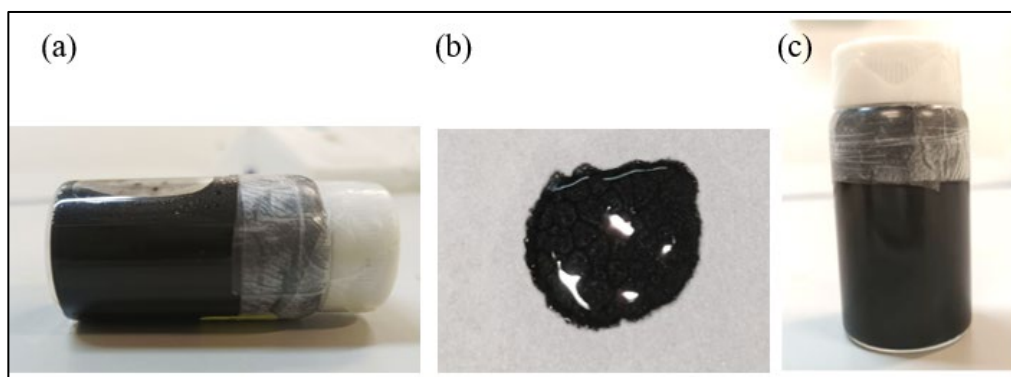
Figure 4.5: GNP/HEC composite (a) as prepared and (b) the texture of ink; (c) composite after 14 days.

The estimated cost for a 20 ml composite (GNP: 0.25 g; HEC: 0.30 g) is RM 11.47 (based on Table 3.1), that is RM 0.57 per ml. Subsequently, the fabricated sensing layer's volume [7.0 cm × 1.0 cm × 24.799 × 10^{-4} cm] is 0.02 ml, the estimated cost is RM 0.01 per sensing layer.

4.3   Sensing Performance of Prototype

4.3.1   Ammonia Gas Response

A pure GNP/HEC composite sensing layer was cut into a small piece (4.0 cm × 1 cm) and laid flat, then connected to an ammonia-sensing tester. In a near-closed environment at room temperature, the sensor was exposed to ammonia concentrations ranging from 15 to 150 ppm. The temporal resistance response during the ammonia gas testing was normalized with respect to the initial resistance.

The results shown in Figure 4.6 indicate that the resistance of the GNP/HEC composite sensing layer increases in the presence of ammonia gas. Three out of five response curves (45, 120, and 150 ppm) increase logarithmically to a peak, which correlates to the diffusion of ammonia gas in

the closed container as it reached saturation. The response curve to 15 ppm recorded an exponential growth attributed to the rapid volatilization of a small volume of ammonia water. Meanwhile, the response curve to 75 ppm recorded a delay in the midst of the growth, attributed to the dripping error of the ammonia water. In practice, the ammonia water that dripped beneath the filter paper affects the fluid dynamics of the ammonia volatile. The majority of the response curves showed longer RCT than RET, indicating that the ammonia molecules process charge transfer via chemisorption to the functional groups (Ghosh et al., 2014). Compared to Ghosh et al. (2014), our prototype showed extended recovery time but no significant shifting in baseline resistance after recovery.
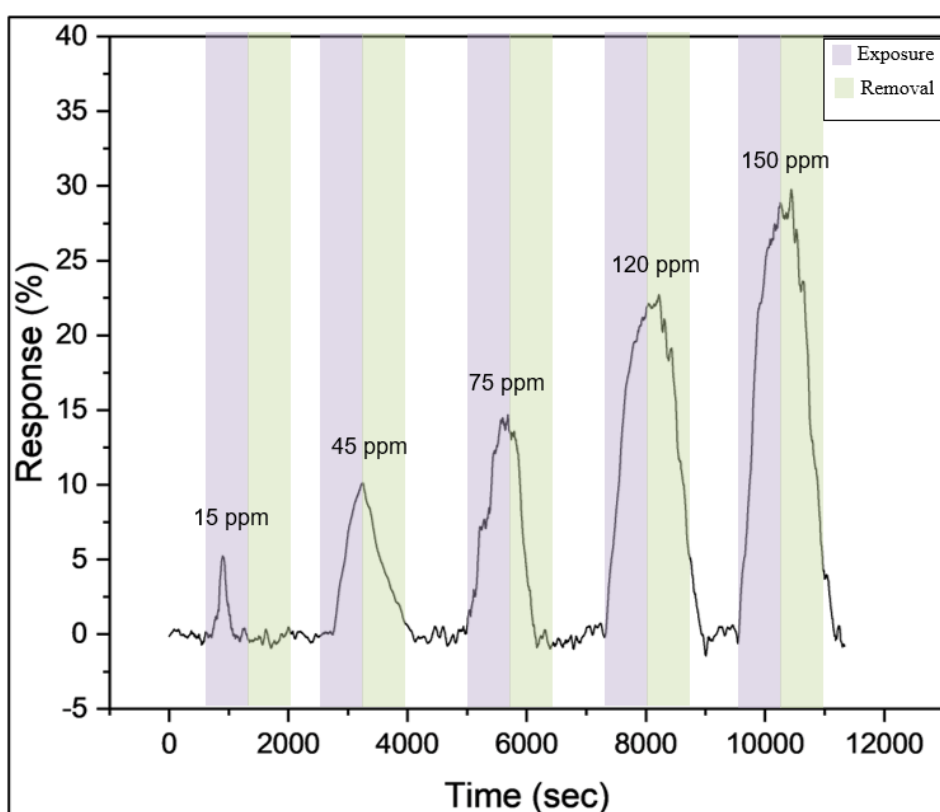
Figure 4.6: Joint graph of resistance response of pure GNP/HEC composite-based sensor in flat geometry to ammonia (NH_3) at five different concentration (15-150 ppm) smoothen by 50-point moving-average.

Additionally, the average signal response to a specific concentration is calculated. Meanwhile the RMS signal, RMS noise and signal-to-noise ratio (SNR) are using the formulae

$$RMS\ signal = \frac{\sqrt{(x_{signal})^2}}{N} \tag{4.1}$$

$$RMS\ noise = \frac{\sqrt{(x_{signal} - x_{ave\text{-}signal})^2}}{N} \tag{4.2}$$

$$SNR = 20\log_{10}\left(\frac{RMS\ signal}{RMS\ noise}\right) \tag{4.3}$$

where

x_{signal} = signal response to a specific level of a stimulus, %

N = sample size

$x_{ave\text{-}signal}$ = average value of x_{signal}, %

A small spreading about the peaks of the temporal response were taken to analyse the signal response. The peaks from 75, 120 and 150 ppm testing were less smooth due to air movement during venting out high concentration of ammonia. Table 4.1 recorded the calculated RMS signal and RMS noise each characterized concentration. The results shown all signal are validated (> 3 dB) to be used for correlation study.

Table 4.1: Statistical analysis of signal and noise in ammonia gas test.

Concentration (ppm)	Mean (%)	RMS signal (%)	RMS noise (%)	Signal-to-noise ratio (dB)	Sample size, N
0	0.0000	-	0.68016	-	4200
15	5.0882	5.1471	0.7765	16.4286	84
45	9.9052	9.9290	0.6862	23.2090	106

Table 4.1 (Continued)

75	14.0104	14.0622	1.2061	21.3332	218
120	22.1072	22.1184	0.7030	29.9558	250
150	28.5248	28.5524	1.2565	27.1297	260

The signal showed linear variation (Adj. R^2 = 0.9957) with the concentration of ammonia gas, ranging from ~ 3 % at 15 ppm to ~ 28 % at 150 ppm, with an intercept at the origin, as shown in Figure 4.7. Based on the correlation study, the sensitivity of the GNP/HEC composite towards ammonia gas was calculated to be 0.1887 % per ppm. Our prototype sensor demonstrated a relatively high sensitivity compared to other sensors such as Yu et al.'s (2011) graphene sheet-based sensor, which showed a sensitivity of 0.0013 % per ppm at 10,000 ppm; Cui et al.'s (2013) rGO sensor surface decorated with silver nanoparticles, which demonstrated a sensitivity of 0.0017 % per ppm at 10,000 ppm; and Ghosh et al.'s (2014) multi-layer rGO on paper substrate, which demonstrated a sensitivity of 0.014 % per ppm at 4000 ppm.
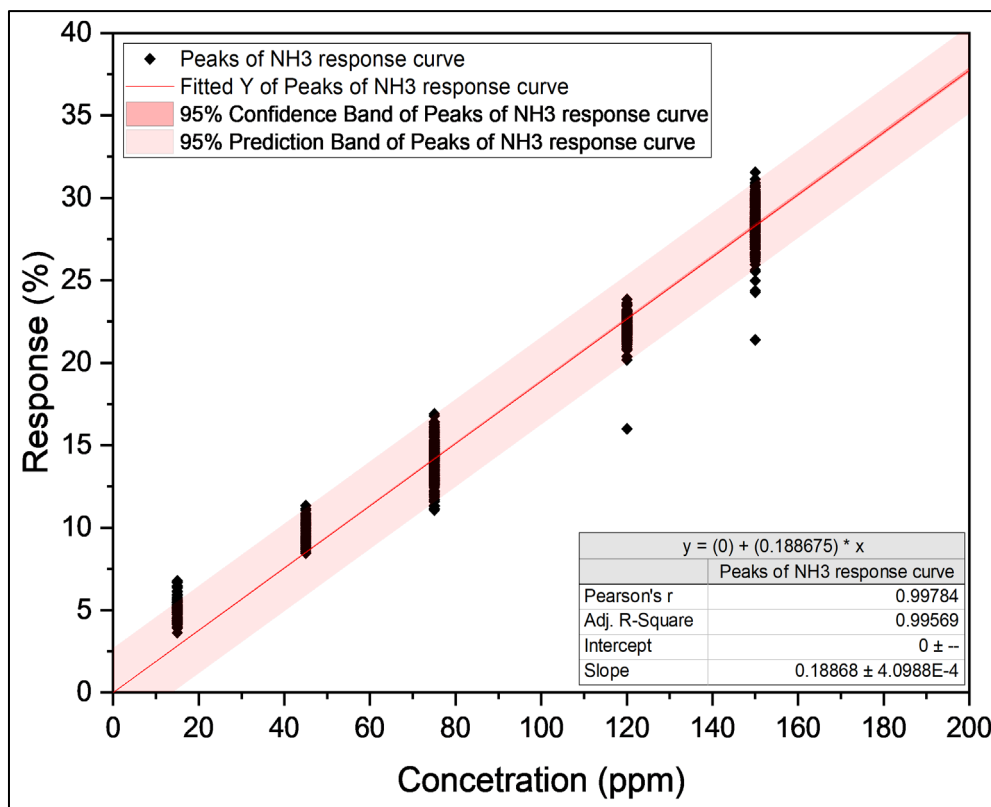
Figure 4.7: Linear regression of resistance response (%) with ammonia concentration (ppm).

Moreover, the RMS noise at ambient calculated 0.6802 % under controlled environment. The limit of detection (LOD) can be calculated using the relation

$$LOD = 3 \times \frac{RMS\ noise_{amb}}{S} \qquad (4.4)$$

The LOD of the prototype ammonia gas sensor was estimated to be 10.8144 ppm. This suggests that the ambient noise attributes to the small amounts of ammonia molecules that are natural part of the air composition. The prototype has a sensitivity and LOD that are comparable to those of the commercial MQ-135 gas sensor. Additionally, the repeatability of the prototype ammonia gas sensor was evaluated by repeating the measurements after a few days using the linear regression model (Response = 0.1887 × concentration), attached in Appendix A. The repeatability evaluation is documented in Table 4.2, which shows that the majority of the detected concentrations were lower than the expected concentrations, indicating the systemic drift error due to degradation

over time. The zero-intercept linear regression model yields a high percentage error in detecting the ammonia concentration released from 100 μl ammonia water. This indicates that the presence of intrinsic ammonia molecules in the air cannot be considered negligible when measuring low concentrations (< 45ppm).

Table 4.2: Measurement of ammonia concentration using the linear regression model.

Volume of NH4OH (μl)	Expected concentration (ppm)	Detected concentration (ppm)	Percentage Error (%)
100	15	31	>+20
300	45	43	-4
500	75	68	-9
800	120	112	-7
1000	150	165	+10

4.3.2   Temperature Response

The prototype GNP/HEC composite temperature sensor, which was passivated by a thin layer of EC/ethanol, was characterized between 38 and 90 °C under room conditions. The prototype was first initialized to average the baseline resistance and then exposed to the heat source until the response reached stagnation, signifying thermal equilibrium. Finally, it was removed from the heat source and left to cool back to room temperature. The resistance response of different temperature tests was normalized to the initial resistance at room conditions (~ 25 °C).

Figure 4.8 displays a first-order characteristic of the prototype temperature sensor. The resistance of the GNP/HEC sensor decreased with increasing temperature displays a typical semiconductor behaviour.
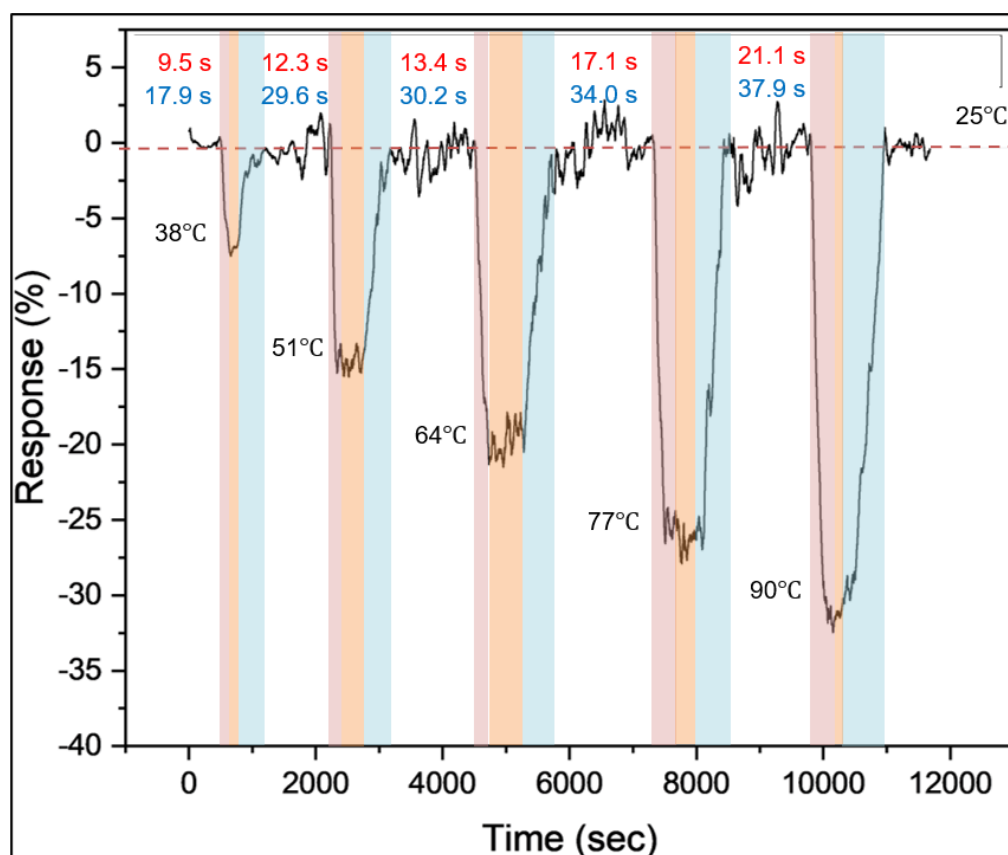
Figure 4.8: Joint graph of resistance response of flexible GNP/HEC composite-based sensor to five different constant heat source (38 - 90 °C) in joint and smoothen by 50-point moving-average. (Legend: (red) heating phase (orange) thermal equilibrium phase; (blue) cooling phase).

The RET and RCT to their final values were determined from the temporal response curves and documented in Table 4.3. Correspondingly, the average response rate was calculated to be 4.3 °C·s^{-1} with a moderate standard deviation of 7 %, supporting the good linearity of the temperature-signal relation. Comparing it to Liu et al. (2018), whose rGO temperature sensor demonstrated a 1.2 s RET from room temperature to 45 °C, the prototype GNP/HEC temperature sensor's RET is relatively slow due to the lack of reduction and EC passivation. Whereas the estimated recovery rate, 2.1 (± 12 %) °C·s^{-1} is half of the response rate. The relatively longer recovery rate could be improved by attaching a heatsink for device development.

Table 4.3: Statistical analysis of the response rate and recovery rate in temperature-sensing test.

Temperature (°C)	Response time (s)	Response rate (°C/s)	Recovery time (s)	Recovery rate (°C/s)
38	9.5	4.0	17.9	2.1
51	12.3	4.1	29.6	1.7
64	13.4	4.8	30.2	2.1
77	17.1	4.5	34.0	2.3
90	21.1	4.3	37.9	2.4
Mean (STD)	-	**4.3 (±7%)**	-	**2.1 (±12%)**

Figure 4.9 illustrates the steady-state sensing condition. A linear variation (Adj. $R^2 = 0.9908$) was observed between temperature and resistance response from approximately -7 % at 38 °C to -30 % at 90 °C. The temperature coefficient of resistance (TCR), calculated to be -0.4938 % per degree Celsius with zero-intercept at 25 °C, was found to be similar to the sensitivity of the prototype sensor. The prototype sensor exhibits 127 % sensitivity relative to commercial PT 100 (|+0.39| % per degree Celsius). However, the prototype sensitivity is 78 % relative to the rGO sensors (|-0.6345|% per degree Celsius) demonstrated by Liu et al. (2018). Nonetheless, both graphene-based sensors exhibit good linearity. Moreover, the prototype temperature sensor's sensitivity is intermediate between that of the solar reduced graphene oxide (SrGO)- and graphene flake-based temperature sensors, |-0.4130| and |-0.7429|% per degree Celsius, respectively (Sahatiya et al., 2016). The authors suggest that the higher TCR is due to more thermally activated defect traps in the disordered structure of the sensitive material, which are responsible for electron hopping over long distances. Additionally, the thermal activated defect traps can be confirmed by measuring the activation energy.
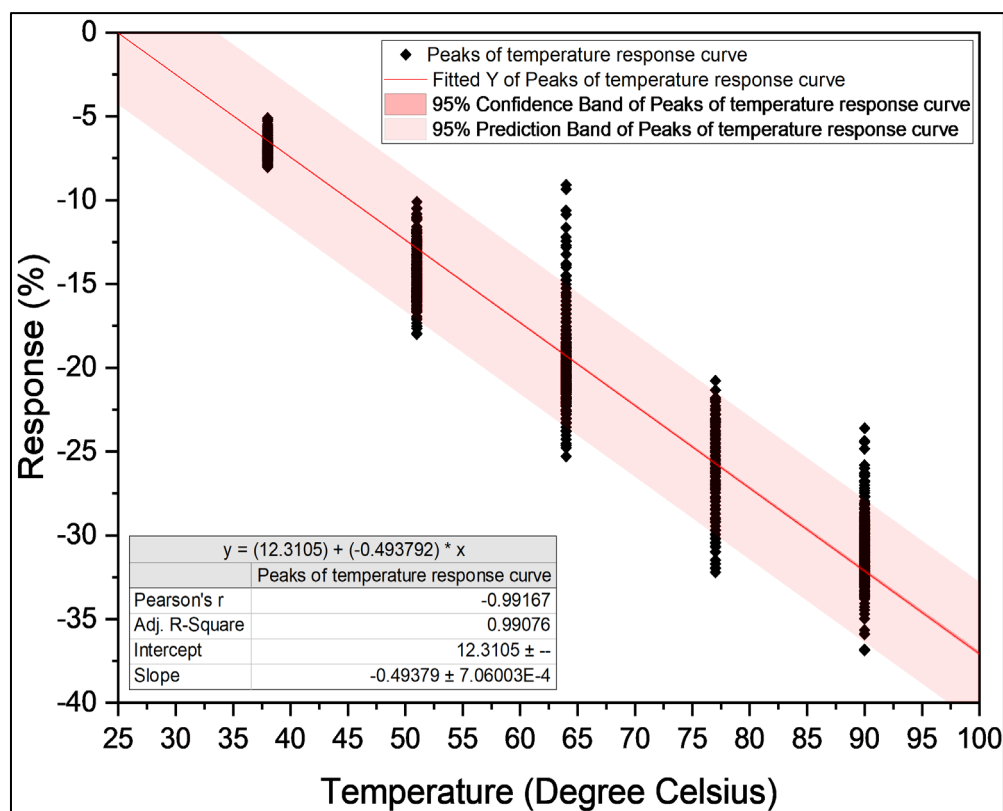
Figure 4.9: Linear regression of resistance response (%) with temperature (°C).

The RMS signal, RMS noise and validation of signals are documented in Table 4.4. The RMS noise are ~ 2 %, attributes to the prototype accuracy equivalent to ± 4 °C [using the relation: RMS noise divided by TCR]. Meanwhile, the RMS ambient noise (25 °C) calculated at 2.6394 % contributes LOD estimated at 16.2208 °C. Higher noise was observed in temperature testing compared ammonia gas testing due to the air movement in the room disrupted the flow of heat to the prototype temperature sensor.

Table 4.4:   Statistical analysis of signal and noise in temperature-sensing test.

Temperature	Mean signal	RMS signal	RMS noise	Signal-to-noise ratio	Sample size,
(°C)	(%)	(%)	(%)	(dB)	N
25	-0.4025	2.6699	2.6394	0.0998	5500
38	-6.8252	6.8509	0.5929	21.2560	205
51	-14.5419	14.6132	1.4416	20.1181	369
64	-19.7419	19.8704	2.2565	18.8953	528

Table 4.4 (Continued)

| 77 | -26.7018 | 26.2671 | 2.1764 | 21.6336 | 390 |
| 90 | -30.6237 | 30.6472 | 1.8540 | 24.3654 | 469 |

4.3.3   Bending Response

The 70 mm prototype flexible bend sensor, passivated by polyimide film, was supported on a flexible plastic substrate and characterized for compression and expansion using a three-point bending setup. For each dataset, the prototype bend sensor was initialized for approximately 1 minute, manually bent and held at the target angle for approximately 1 minute, and finally relaxed for approximately 1 minute. The resistance responses were normalized by the initial resistance for each trial of testing. The bending test was repeated in ascending order of the bending angle, from the compression state to the expansion state. The flat resistance over 12 trials averaged at 105 (± 3 %) kΩ can be found in Appendix A.

Figure 4.10 illustrates the temporal response of the prototype bend sensor. The signal to bending reflects instant RET and RCT showing zero-order time-dependent characteristic to data acquisition (scanning time: 60 ms). The results show decreased resistance response to compression while increased resistance response to expansion. The resistance response to the polarity of bending agrees with the laser-induced graphene (LIG) sensor demonstrated by Kulyk et al. (2021). The authors support that the overall resistance behaviour to bending can be contributed by the intrinsic piezoresistivity of GNPs and the overlapping area of GNP-HEC fibres. The macro-scale GNP-HEC fibres sensing mechanism is dominant in explaining the saturation resistance response behaviour where the conductive fibres are overlapped (or separated) far enough to correspond to the compression limit (or expansion limit). Nevertheless, the bending response of the GNP/HEC bend sensor is reversible, and there is no significant increment of noise nor zero-drift over 11 cycles of bending tests with ascending bending angles compared to previous work. Figure 4.11 presents the range of measurement from 16 kΩ to 112 kΩ, equivalent to -84 % to +7 % relative response to flat geometry. The bending response can be generalized using a 5th order polynomial equation (Adj. R^2 = 0.9962) relevant to -70° to +60°. However, it

is clear that the response phase-out from compression -60° below and expansion +20° above.
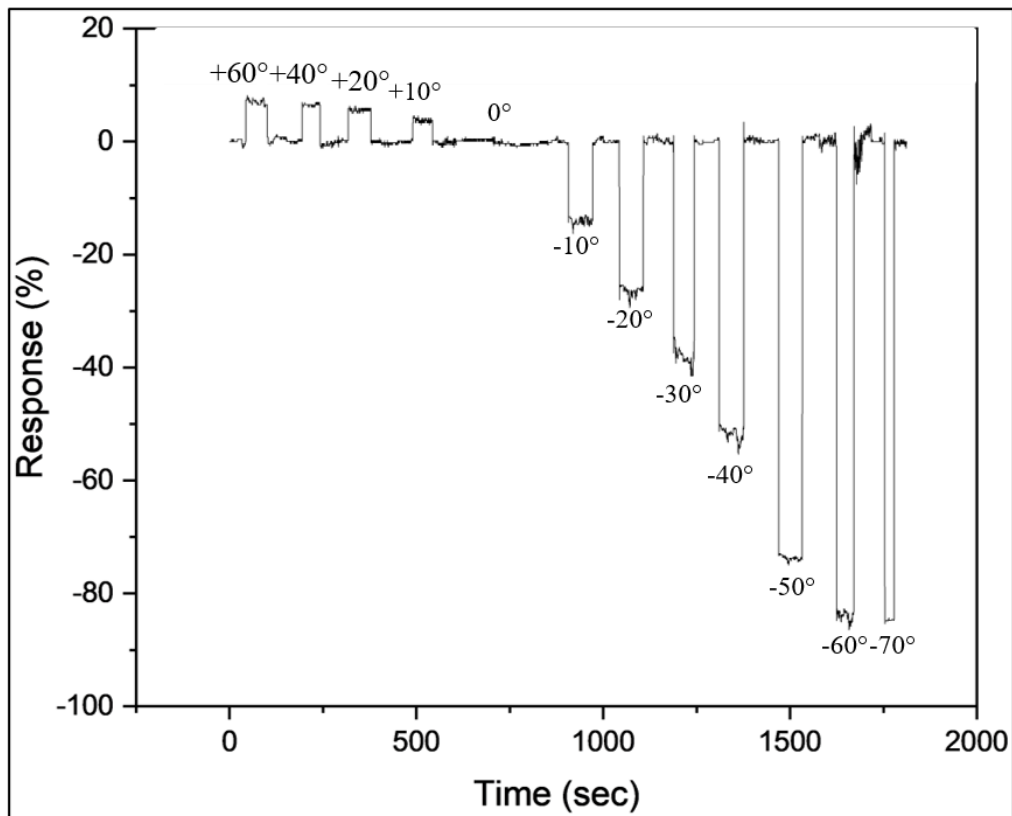
Figure 4.10:   Joint graph of resistance response of flexible GNP/HEC composite-based sensor to three-point bending (+60° to -70°).
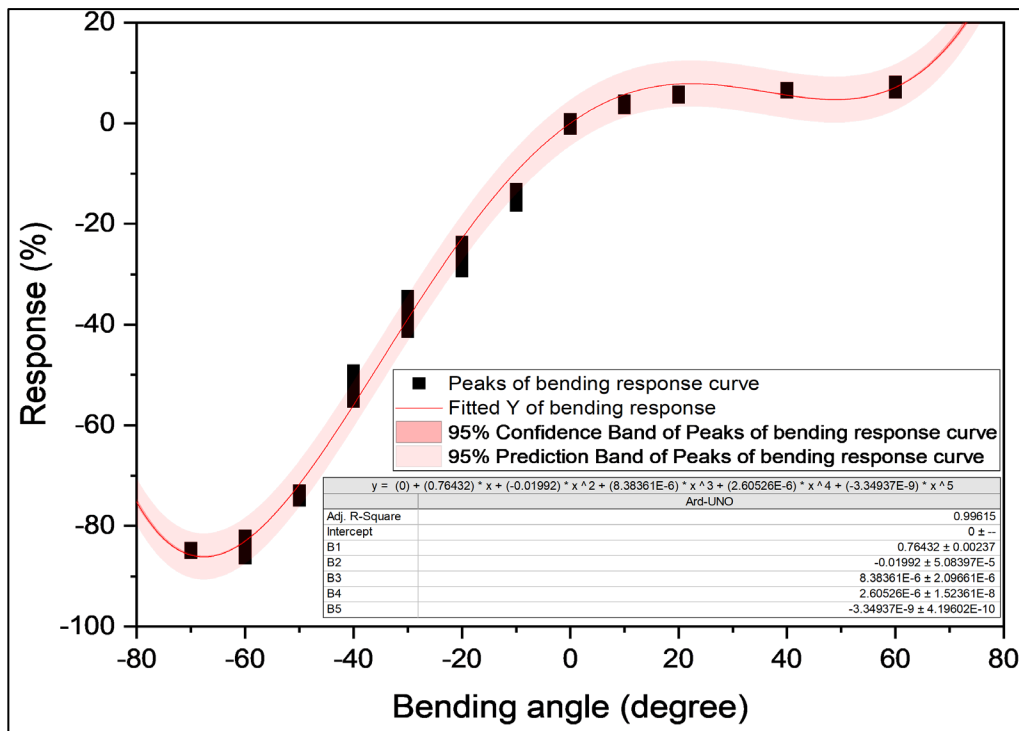
Figure 4.11: Polynomial regression of resistance response (%) with bending angle (°).

The prototype exhibits higher sensitivity and a wider detection range for compression than for expansion, due to the single-sided sensing layer or the polyimide tape limiting the separation of GNP-HEC fibres. Therefore, it is practical to consider only the compression signal. Figure 4.12 shows the linear variation (Adj-R^2: 0.9983) between the resistance response and compression angle within -60° to 0°. The prototype displays a high sensitivity (1.3851 % per degree angle) attributed to the intrinsic piezoresistivity of GNPs' strain-induced pseudo magnetic field characteristics. This high sensitivity indicates a useful application to detect or sense tiny motions without signal amplification.
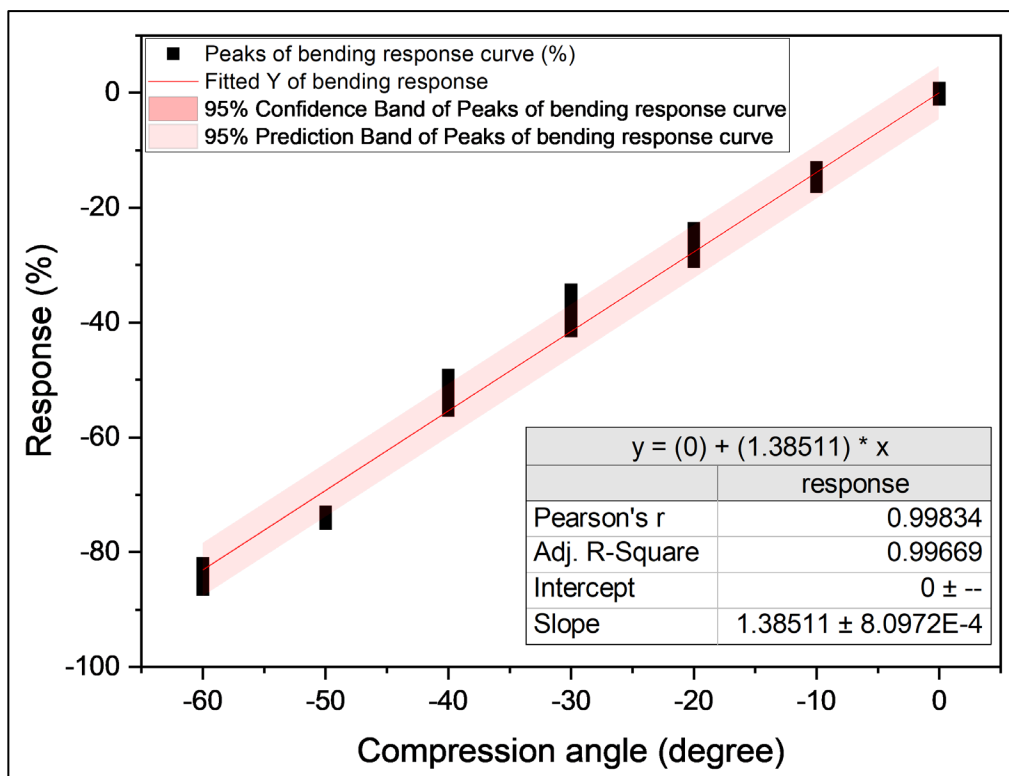
Figure 4.12:   Linear variation of response and compression angle.

The overall prototype's signal to bending is low noise and able to sustain stably (as shown in Table 4.5). Essentially, the prototype exhibits insignificant noise at flat geometry (0.4072 %). Moreover, the LOD calculated at 0.8819° indicating potential to sense tiny deflective strain.

Table 4.5:   Statistical analysis of signal and noise in bending test.

Bending angle (°)	Mean signal (%)	RMS signal (%)	RMS noise (%)	Signal-to-noise ratio (dB)	Sample size, N
-70	-84.7493	84.7494	0.1195	57.0167	419
-60	-83.9676	83.9717	0.8303	40.0979	780
-50	-73.7538	73.7549	0.3954	45.4158	1049
-40	-51.8058	51.8184	1.1427	33.1313	1100
-30	-38.1658	38.1979	1.5643	27.7545	917
-20	-26.4357	26.4482	0.8142	30.2332	1073
-10	-14.0839	14.0970	0.6077	27.3088	1065
0	-0.1639	0.4289	0.4072	0.65233	3748

Table 4.5 (Continued)

+10	3.7179	3.7304	0.3051	21.7466	886
+20	5.5571	5.5626	0.2468	27.0574	1008
+40	6.4855	6.4891	0.2147	29.6052	803
+60	7.0089	7.0231	0.4461	23.9413	962

4.3.4   Respiration Monitoring

The prototype respiration monitoring sensor was placed in a flat position and tested for human respiration under room conditions. The test was repeated until the response completely recovered to a stagnant state, with a total of 15 respiration cycles tested to obtain the average respiration signal and repeatability.

Figure 4.13 displays the resistance response in the time domain for 15 continuous respiration cycles. The prototype was able to produce a rhythmic signal corresponding to respiration. The baseline shifted up by 2 % at the end of the respiration test, indicating humidity hysteresis caused by the high relative humidity during respiration (>55 % RH), which increases the interlayer spacing between the graphene sheets (Lv et al., 2019). Thus, the effect of humidity on interlayer spacing results in a saturation sensing region when the interlayer spacing is expanded far enough. The hysteresis effect demonstrated moderate linear variation with the number of cycles, as detailed in Appendix A. However, the humidity hysteresis can be reset by heating (e.g., 75°C for 30 min), and no effect on the sensing response was demonstrated by Naik and Krishnaswamy (2016).
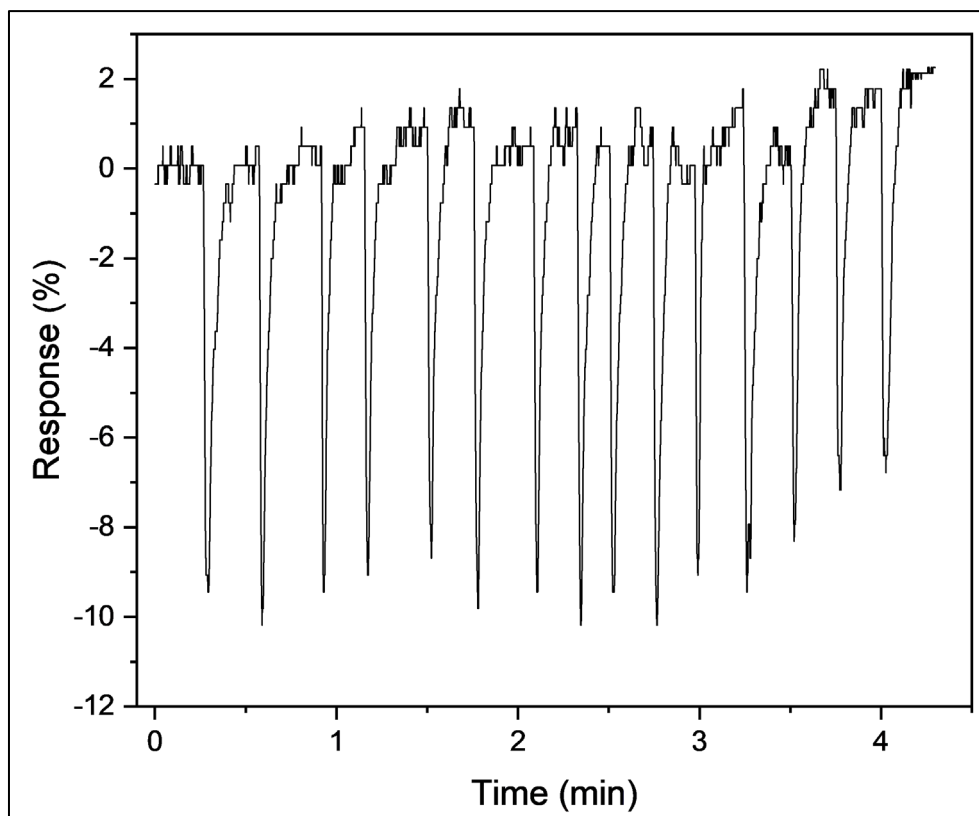
Figure 4.13: Temporal response of 15 cycles of exhalation detection.

Table 4.6 documented the average RET of the respiration monitoring modal to final value 1.18 (± 19 %) seconds. Meanwhile, the average RCT to baseline measured at 4.45 (± 21 %) seconds is 377 % of response time, under regular air movement at room conditions. The GNP/HEC composite's RET is similar to the CB/rGO mixture by Liu et al. (2019a) supported the sufficient response time to regular human respiration.

Table 4.6: Statistical analysis of response time and recovery time in respiration monitoring test.

Count	Response time (s)	Recovery time (min)
1	1.80	5.34
2	1.14	6.42
3	1.02	3.18
4	1.02	3.66
5	1.38	3.96
6	1.32	4.44
7	1.32	4.38
8	1.32	5.10
9	1.08	4.74

Table 4.6 (Continued)

10	1.26	5.04
11	1.02	3.00
12	1.20	5.52
13	1.02	3.60
14	0.96	3.72
15	0.90	4.68
Mean (STD)	**1.18 (± 19 %)**	**4.45 (± 21 %)**

Table 4.7 documents the ambient noise and exhalation signals identified from the measurements. The RMS noise and RMS signal over 15 samples were 0.6948 % and 9.8783 %, respectively. The average signal-to-noise ratio calculated at 23.0561 dB is sufficient to distinguish the respiration signal. The signal threshold was estimated at 0.21 RMS signal [2.0844 % = 3 times the RMS noise], corresponding to a response time threshold of 0.25 seconds and a recovery time threshold of 0.93 seconds. By projecting the signal threshold, the prototype is capable of monitoring fast-paced respiration rates, such as the breathing rate of COVID-19 patients, which is reported to be 20 breaths per minute or 3.75 seconds per breath (Lubecke et al., 2021).

Table 4.7: Statistical analysis of signal and noise in respiration monitoring test.

Sample	Average baseline (%)	Noise (%)	Actual noise (%)	Dipl (%)	Actual dip (%)
1	0.0020	0.5000	0.4977	-9.4399	-9.4399
2	0.1090	0.5000	0.3910	-10.1813	-10.1813
3	0.2800	0.9251	0.6447	-9.4399	-9.4399
4	0.3120	1.3528	1.0406	-9.0664	-9.9915
5	0.5440	1.3528	0.8084	-8.6911	-9.6162
6	1.1450	1.7829	0.6376	-9.8115	-10.7366
7	0.3770	0.9251	0.5484	-9.4399	-9.9399
8	0.7440	1.3528	0.6083	-10.1813	-11.1064
9	0.5000	0.9251	0.4254	-9.4399	-9.9399
10	0.6210	1.3528	0.7323	-10.1813	-11.1064
11	0.1000	0.9251	0.8252	-9.0664	-9.0664
12	0.6990	1.7829	1.0839	-9.4399	-10.7927
13	0.3610	0.9251	0.5641	-8.3138	-8.8138
14	1.5870	2.2153	0.6279	-7.1704	-8.9533
15	1.4960	0.9251	-0.5714	-6.7853	-8.5682
16	2.0470	-	-	-	-
RMS	**-**	**-**	**0.6948**	**-**	**9.8783**

To compare, the RMS respiration signal is higher (198 %) than the predicted signal of the prototype temperature sensor (<|-5| %) for the temperature of human exhalation at 34 – 37 °C. It is suspected that the prototype respiration-monitoring sensor also responds to the humidity in exhaled air, causing further decreases in resistance response. The decrease in resistance with increased humidity indicates the substantial defects in graphene sheets. Additionally, the findings show that the composite would marginally suppress the ammonia response at higher relative humidity, indicating better selectivity towards ammonia.

4.4 Potential Applications

The findings indicate that the graphene/cellulose composite can produce distinguishable signals based on signal polarity and/or time-dependent characteristics. Table 4.8 summarized the potential implementations of flexible and multimodal sensing graphene/cellulose composite and its applications in real-life. Moreover, Liu et al. (2019a) demonstrated that a single patch of flexible multimodal sensor can collect and differentiate two signals simultaneously. The authors tested the sensing performance of the sensor on a combination of temperature and pressure, as well as a combination of humidity and strain. The secondary signal (e.g., temperature or humidity) reflects on the baseline shifting and can be measured by the deviation from the standard baseline, while the primary signal (e.g., pressure or strain) reflects on the relative response to the current baseline. The strain/pressure has minimal effect on the temperature/humidity signal accuracy. Furthermore, Lee et al. (2021) demonstrated the implementation of a support vector machine (SVM) algorithm to recognize the pattern of pressure/strain based on throat movement, such as coughing, humming, nodding, and swallowing.

However, this framework is only applicable to primary signals with zero-order characteristics overlaid on secondary signals with first- or higher-order characteristics. On the other hand, Hua et al. (2018) introduced the concept of an integrated sensor where different customized modalities of sensors are fabricated in an array or matrix format with close proximity. Additionally, Díez-Pascual and Rahdar (2022) suggested the preparation of a

flexible sensing layer using direct roll printing onto flexible printed electronic circuits. Hence, passivation can be a practical technique to differentiate the signal by adjusting the selectivity of a targeted signal. Nonetheless, the experimented passivation in the project has shown that it can affect the sensing performance of pure sensing layers, such as the RET of the prototype temperature sensor and the limited measurement range in the expansion state of the prototype bend sensor. Proposed improvements such as investigating a hydrophobic GNP/EC composite for temperature-sensing modalities, rather than additional waterproof coating (Mardi, Risi Ambrogioni and Reale, 2020). Secondly, a double-sided GN/HEC bend sensor for equal directional response, amplification of signal, and elimination of common signals (Kaidarova et al., 2019).

Following the resolution of the complexity in detecting multiple stimuli, the real-life applications of flexible graphene/cellulose composites for multimodal sensing are anticipated. For example, Alam et al. (2020) demonstrated a flexible multimodal sensor attached to a commercial dust mask that provides signals from respiration and even ammonia gas, enabling safety monitoring in industry. The graphene/cellulose composite can also be fabricated onto a textile yarn substrate to be attached to medical coats or workwear to detect ammonia leakage (Singh, Meyyappan and Nalwa, 2017). Moreover, Bi et al. (2020) demonstrated various wearable sensors based on rGO fabric to capture human motion, such as joint bending, forearm muscle contraction, and breathing motion on the chest. Xie et al. (2020) supported the inherent high sensitivity of flexible graphene-based sensors, which are able to detect wrist pulses, throat vibrations, and facial muscle tension. Nag et al. (2022) proposed the use of a flexible graphene temperature sensor to monitor human body temperature as an indicator of personal emotional state to aid in psychological studies. The authors also proposed implementing the sensor on robot fingertips for real-time sensing, supported by Bluetooth wireless transmission.

Table 4.8: Reviews of implementations and potential real-life applications of flexible graphene/cellulose composite for multimodal sensing.

Sources	Implementations/Potential Applications
Liu et al. (2019a)	Flexible graphene-based sensor to sense two stimuli simultaneously.
Lee et al. (2021)	SVM algorithm to detect human motion based on strain signal.
Hua et al. (2018)	Integrated sensor.
Díez-Pascual and Rahdar (2022)	Direct roll printing for flexible sensors device.
Mardi, Risi Ambrogioni and Reale (2020)	Functionalized matrix for graphene-based sensing composite.
Kaidarova et al. (2019).	Bilayer sensors with opposing inputs.
Singh, Meyyappan and Nalwa, (2017), Alam et al. (2020)	Graphene-based sensory textiles for breath monitoring and ammonia gas leakage detection.
Bi et al. (2020)	Wearable sensors for human motion monitoring.
Xie et al. (2020)	Ultra-sensitive wearable sensors for human health monitoring.
Nag et al. (2022)	Wearable temperature sensors for psychological studies.
Nag et al. (2022)	Wireless wearable multifunctional sensors for robotics applications.

CHAPTER 5

CONCLUSIONS AND RECOMMENDATIONS

5.1   Conclusions

A low-cost sensing ink based on GNP/HEC composite (raw material of sensing layer: 7.0 mm × 1.0 mm, cost: RM 0.01) was synthesized via a low-temperature colloidal processing method (i.e., ultrasonication and hotplate stirrer) and fabricated as a flexible multimodal sensing sensor using a scalable delivery technique (i.e., solution approach and brush coating). EDX/SEM confirmed the graphene oxide flakes stacked on HEC fibres formed a thick and homogenous network structure, showing the good binding and dispersing effect of the polymer matrix. The prototype sensing layer displays low conductivity and nominal resistance of ~100 kOhm as a resistive sensor. The prototype ammonia sensor characterized from 15 to 150 ppm exhibits moderate sensitivity (0.1887 % per ppm) with good linearity while and LOD (11 ppm), and the sensing performance is reversible. The prototype temperature sensor characterized from 38 to 90 °C at room condition, displays high sensitivity (-0.4938 % per degree Celsius) with good linearity, lower response rate (4.1 °C·s^{-1}), moderate accuracy ($\pm$ 4 °C) and LOD (16.2208 °C). The prototype bend sensor exhibits instant response (< 60 ms) practical range of measurement (16 ~ 112 kΩ), high sensitivity to compression (1.3851 % per degree angle), LOD (0.8819°) and stable signal in compression state. The prototype respiration monitoring sensor exhibits a high signal-to-noise ratio (23.0561 dB), threshold signal (2.0844 %), practical response time (1.18 s) and recovery time (4.45 s). However, hysteresis (+ 2 %) is observed over 15 cycles of respiration.

The project has achieved its objective of demonstrating the potential of using a graphene/cellulose composite for flexible and multimodal sensing. The prototype sensing ink was able to detect multiple stimuli simultaneously and could be further developed as an integrated sensor with the assistance of passivation techniques and analytical algorithms.

5.2 Recommendations for Future Work

There are three areas where future improvements can be made to enhance the GNP/HEC sensing ink: accuracy, reliability, and applications. To improve the prototype's accuracy, the composite recipe can be optimized by reducing the oxygen content and creating a smoother GNP/HEC network structure with fewer defects that cause intrinsic noise. A better delivery method, such as screen printing or rolling, should be adopted to improve the uniformity of the sensing layer. More characterization tools, such as Raman spectroscopy, XRD, and FTIR, should be used to investigate the effect of composite material properties on its sensing performance.

For the reliability aspect, the prototype testing should be conducted under various environmental conditions to evaluate their effect on the sensing performance. Concurrently, a reliability analysis of the prototype sensing layer from a production batch should be conducted to standardize specifications and aid in commercialization in the near future.

Finally, the sensing layer can be investigated on other flexible and robust substrates, such as elastomers and fabrics. The sensing layer should be incorporated with flexible circuits and wireless signal transmission to allow prototype testing in dynamic real-life environments and develop service-oriented studies of the sensing ink to address the need of potential customers.

REFERENCES

Abdel-Halim, E.S., 2014. Chemical modification of cellulose extracted from sugarcane bagasse: Preparation of hydroxyethyl cellulose. *Arabian Journal of Chemistry*, 7(3), pp.362–371. https://doi.org/10.1016/j.arabjc.2013.05.006.

Abid, P., Sehrawat, S.S., Islam, M. and Ahmad, S., 2018. Reduced graphene oxide (rGO) based wideband optical sensor and the role of Temperature, Defect States and Quantum Efficiency OPEN. [online] 8. https://doi.org/10.1038/s41598-018-21686-2.

Alam, M.M., Lee, S., Kim, M., Han, K.S., Cao, V.A. and Nah, J., 2020. Ultra-flexible nanofiber-based multifunctional motion sensor. *Nano Energy*, 72. https://doi.org/10.1016/j.nanoen.2020.104672.

Anwer, A.H., Khan, N., Ansari, M.Z., Baek, S.S., Yi, H., Kim, S., Noh, S.M. and Jeong, C., 2022. *Recent Advances in Touch Sensors for Flexible Wearable Devices*. *Sensors*, https://doi.org/10.3390/s22124460.

Balandin, A.A., 2011. *Thermal Properties of Graphene, Carbon Nanotubes and Nanostructured Carbon Materials*.

Balandin, A.A., Ghosh, S., Bao, W., Calizo, I., Teweldebrhan, D., Miao, F. and Lau, C.N., 2008. Superior thermal conductivity of single-layer graphene. *Nano Letters*, 8(3), pp.902–907. https://doi.org/10.1021/nl0731872.

Benyounes, K., Remli, S. and Benmounah, A., 2018. Rheological behavior of Hydroxyethylcellulose (HEC) Solutions. In: *Journal of Physics: Conference Series*. Institute of Physics Publishing. https://doi.org/10.1088/1742-6596/1045/1/012008.

Bi, S., Hou, L., Dong, W. and Lu, Y., 2021. Multifunctional and Ultrasensitive-Reduced Graphene Oxide and Pen Ink/Polyvinyl Alcohol-Decorated Modal/Spandex Fabric for High-Performance Wearable Sensors. *ACS Applied Materials and Interfaces*, 13(1), pp.2100–2109. https://doi.org/10.1021/acsami.0c21075.

Blažková, A., Hrivíková, J. and Lapčík, L., 1990. *Viscosity properties of aqueous solutions of hydroxyethylcellulose*.

Bunch, J.S., Verbridge, S.S., Alden, J.S., Van Der Zande, A.M., Parpia, J.M., Craighead, H.G. and Mceuen, P.L., 2008. *Impermeable Atomic Membranes from Graphene Sheets*.

Cao, M.S., Wang, X.X., Cao, W.Q. and Yuan, J., 2015. Ultrathin graphene: electrical properties and highly efficient electromagnetic interference shielding. *Journal of Materials Chemistry C*, 3(26), pp.6589–6599. https://doi.org/10.1039/c5tc01354b.

Cui, S., Mao, S., Wen, Z., Chang, J., Zhang, Y. and Chen, J., 2013. Controllable synthesis of silver nanoparticle-decorated reduced graphene oxide hybrids for ammonia detection. *Analyst*, [online] 138(10), pp.2877–2882. https://doi.org/10.1039/C3AN36922F.

Dang Luong, N., Pahimanolis, N., Hippi, U., Korhonen, J.T., Ruokolainen, J., Johansson, L.-S., Nam, J.-D. and Seppälä, J., 2011. Graphene/cellulose nanocomposite paper with high electrical and mechanical performances. [online] https://doi.org/10.1039/c1jm12134k.

Davidovich-Pinhas, M., Barbut, S. and Marangoni, A.G., 2015. The gelation of oil using ethyl cellulose. *Carbohydrate Polymers*, 117, pp.869–878. https://doi.org/10.1016/j.carbpol.2014.10.035.

Díez-Pascual, A.M. and Rahdar, A., 2022. *Graphene-Based Polymer Composites for Flexible Electronic Applications*. *Micromachines*, https://doi.org/10.3390/mi13071123.

Dong, L., Yang, J., Chhowalla, M. and Loh, K.P., 2017. *Synthesis and reduction of large sized graphene oxide sheets*. *Chemical Society Reviews*, https://doi.org/10.1039/c7cs00485k.

El Fawal, G.F., Abu-Serie, M.M., Hassan, M.A. and Elnouby, M.S., 2018. Hydroxyethyl cellulose hydrogel for wound dressing: Fabrication, characterization and in vitro evaluation. *International Journal of Biological Macromolecules*, 111, pp.649–659. https://doi.org/10.1016/j.ijbiomac.2018.01.040.

Fu, X., Li, G., Cai, S., Yang, H., Lin, K., He, M., Wen, J., Li, H., Xiong, Y., Chen, D. and Liu, X., 2021. Color-switchable hybrid dots/hydroxyethyl cellulose ink for anti-counterfeiting applications. *Carbohydrate Polymers*, 251. https://doi.org/10.1016/j.carbpol.2020.117084.

Fujii, S. and Enoki, T., 2013. Rearrangement of π-electron network and switching of edge-localized π state in reduced graphene oxide. *ACS Nano*, 7(12), pp.11190–11199. https://doi.org/10.1021/nn404937z.

Ghosh, R., Singh, A., Santra, S., Ray, S.K., Chandra, A. and Guha, P.K., 2014. Highly sensitive large-area multi-layered graphene-based flexible ammonia sensor. *Sensors and Actuators, B: Chemical*, 205, pp.67–73. https://doi.org/10.1016/j.snb.2014.08.044.

Habibi, Y., 2014. *Key advances in the chemical modification of nanocelluloses*. *Chemical Society Reviews*, https://doi.org/10.1039/c3cs60204d.

Han, Y., Xu, Z. and Gao, C., 2013. Ultrathin graphene nanofiltration membrane for water purification. *Advanced Functional Materials*, 23(29), pp.3693–3700. https://doi.org/10.1002/adfm.201202601.

Haroun, A., Le, X., Gao, S., Dong, B., He, T., Zhang, Z., Wen, F., Xu, S. and Lee, C., 2021. *Progress in micro/nano sensors and nanoenergy for future*

AIoT-based smart home applications. Nano Express, https://doi.org/10.1088/2632-959X/abf3d4.

Ho, H.N., Le, H.H., Le, T.G., Duong, T.H.A., Ngo, V.Q.T., Dang, C.T., Nguyen, V.M., Tran, T.H. and Nguyen, C.N., 2022. Formulation and characterization of hydroxyethyl cellulose-based gel containing metronidazole-loaded solid lipid nanoparticles for buccal mucosal drug delivery. *International Journal of Biological Macromolecules*, 194, pp.1010–1018. https://doi.org/10.1016/J.IJBIOMAC.2021.11.161.

Hua, Q., Sun, J., Liu, H., Bao, R., Yu, R., Zhai, J., Pan, C. and Wang, Z.L., 2018. Skin-inspired highly stretchable and conformable matrix networks for multifunctional sensing. *Nature Communications 2018 9:1*, [online] 9(1), pp.1–11. https://doi.org/10.1038/s41467-017-02685-9.

Huang, X., Leng, T., Georgiou, T., Abraham, J., Raveendran Nair, R., Novoselov, K.S. and Hu, Z., 2018. Graphene Oxide Dielectric Permittivity at GHz and Its Applications for Wireless Humidity Sensing. *Scientific Reports 2017 8:1*, [online] 8(1), pp.1–7. https://doi.org/10.1038/s41598-017-16886-1.

Irani, F.S., Shafaghi, A.H., Tasdelen, M.C., Delipinar, T., Kaya, C.E., Yapici, G.G. and Yapici, M.K., 2022. Graphene as a Piezoresistive Material in Strain Sensing Applications. *Micromachines 2022, Vol. 13, Page 119*, [online] 13(1), p.119. https://doi.org/10.3390/MI13010119.

Kaidarova, A., Khan, M.A., Marengo, M., Swanepoel, L., Przybysz, A., Muller, C., Fahlman, A., Buttner, U., Geraldi, N.R., Wilson, R.P., Duarte, C.M. and Kosel, J., 2019. Wearable multifunctional printed graphene sensors. *npj Flexible Electronics 2019 3:1*, [online] 3(1), pp.1–10. https://doi.org/10.1038/s41528-019-0061-5.

Khalifa, M., Wuzella, G., Lammer, H. and Mahendran, A.R., 2020. Smart paper from graphene coated cellulose for high-performance humidity and piezoresistive force sensor. *Synthetic Metals*, 266. https://doi.org/10.1016/J.SYNTHMET.2020.116420.

Khan, Y., Ostfeld, A.E., Lochner, C.M., Pierre, A. and Arias, A.C., 2016. *Monitoring of Vital Signs with Flexible and Wearable Medical Devices. Advanced Materials*, https://doi.org/10.1002/adma.201504366.

Kim, B.J., Jang, H., Lee, S.K., Hong, B.H., Ahn, J.H. and Cho, J.H., 2010. High-performance flexible graphene field effect transistors with ion gel gate dielectrics. *Nano Letters*, 10(9), pp.3464–3466. https://doi.org/10.1021/NL101559N.

Klemm, D., Heublein, B., Fink, H.P. and Bohn, A., 2005. Cellulose: fascinating biopolymer and sustainable raw material. *Angewandte Chemie (International ed. in English)*, [online] 44(22), pp.3358–3393. https://doi.org/10.1002/ANIE.200460587.

Kulyk, B., Silva, B.F.R., Carvalho, A.F., Silvestre, S., Fernandes, A.J.S., Martins, R., Fortunato, E. and Costa, F.M., 2021. Laser-Induced Graphene from Paper for Mechanical Sensing. *ACS Applied Materials and Interfaces*, [online] 13(8), pp.10210–10221. https://doi.org/10.1021/ACSAMI.0C20270.

Lee, C., Wei, X., Kysar, J.W. and Hone, J., 2008. Measurement of the elastic properties and intrinsic strength of monolayer graphene. *Science*, 321(5887), pp.385–388. https://doi.org/10.1126/science.1157996.

Lee, J.H., Chee, P.S., Lim, E.H. and Tan, C.H., 2021. Artificial intelligence-assisted throat sensor using ionic polymer–metal composite (IPMC) material. *Polymers*, 13(18). https://doi.org/10.3390/polym13183041.

Levy, N., Burke, S.A., Meaker, K.L., Panlasigui, M., Zettl, A., Guinea, F., Castro Neto, A.H. and Crommie, M.F., 2010. Strain-induced pseudo-magnetic fields greater than 300 tesla in graphene nanobubbles. *Science*, [online] 329(5991), pp.544–547. https://doi.org/10.1126/SCIENCE.1191700/SUPPL_FILE/LEVY.SOM.PDF.

Li, N., Chen, Z., Ren, W., Li, F. and Cheng, H.M., 2012a. Flexible graphene-based lithium ion batteries with ultrafast charge and discharge rates. *Proceedings of the National Academy of Sciences of the United States of America*, [online] 109(43), pp.17360–17365. https://doi.org/10.1073/PNAS.1210072109/SUPPL_FILE/SAPP.PDF.

Li, Y.J., Sun, Q.Q., Chen, L., Zhou, P., Wang, P.F., Ding, S.J. and Zhang, D.W., 2012b. Hexagonal boron nitride intercalated multi-layer graphene: A possible ultimate solution to ultra-scaled interconnect technology. *AIP Advances*, [online] 2(1), p.12191. https://doi.org/10.1063/1.3701267/21761.

Liang, R., Luo, A., Zhang, Z., Li, Z., Han, C. and Wu, W., 2020. Research progress of graphene-based flexible humidity sensor. *Sensors (Switzerland)*, 20(19), pp.1–17. https://doi.org/10.3390/s20195601.

Liu, G., Tan, Q., Kou, H., Zhang, L., Wang, J., Lv, W., Dong, H. and Xiong, J., 2018. A flexible temperature sensor based on reduced graphene oxide for robot skin used in internet of things. *Sensors (Switzerland)*, 18(5). https://doi.org/10.3390/s18051400.

Liu, H., Xiang, H., Wang, Y., Li, Z., Qian, L., Li, P., Ma, Y., Zhou, H. and Huang, W., 2019a. A Flexible Multimodal Sensor That Detects Strain, Humidity, Temperature, and Pressure with Carbon Black and Reduced Graphene Oxide Hierarchical Composite on Paper. *ACS Applied Materials and Interfaces*, [online] 11(43), pp.40613–40619. https://doi.org/10.1021/ACSAMI.9B13349/SUPPL_FILE/AM9B13349_SI_002.AVI.

Liu, Y., Liu, L., Li, Z., Zhao, Y. and Yao, J., 2019b. Green and facile fabrication of smart cellulose composites assembled by graphene nanoplates for dual sensing. *Cellulose*, [online] 26(17), pp.9255–9268. https://doi.org/10.1007/S10570-019-02735-Z/METRICS.

Lubecke, L.C., Ishmael, K., Zheng, Y., Boric-Lubecke, O. and Lubecke, V.M., 2021. Identification of COVID-19 Type Respiratory Disorders Using Channel State Analysis of Wireless Communications Links; Identification of COVID-19 Type Respiratory Disorders Using Channel State Analysis of Wireless Communications Links. *2021 43rd Annual International Conference of the IEEE Engineering in Medicine & Biology Society (EMBC)*. https://doi.org/10.1109/EMBC46164.2021.9630016.

Lv, C., Hu, C., Luo, J., Liu, S., Qiao, Y., Zhang, Z., Song, J., Shi, Y., Cai, J. and Watanabe, A., 2019. Recent Advances in Graphene-Based Humidity Sensors. *Nanomaterials 2019, Vol. 9, Page 422*, [online] 9(3), p.422. https://doi.org/10.3390/NANO9030422.

Mardi, S., Risi Ambrogioni, M. and Reale, A., 2020. Developing printable thermoelectric materials based on graphene nanoplatelet/ethyl cellulose nanocomposites. *Materials Research Express*, 7(8). https://doi.org/10.1088/2053-1591/ababc0.

Mayorov, A.S., Gorbachev, R. V, Morozov, S. V, Britnell, L., Jalil, R., Ponomarenko, L.A., Blake, P., Novoselov, K.S., Watanabe, K., Taniguchi, T. and Geim, A.K., 2011. Micrometer-Scale Ballistic Transport in Encapsulated Graphene at Room Temperature.

Melios, C., Giusca, C.E., Panchal, V. and Kazakova, O., n.d. Water on graphene: Review of recent progress.

Myasoedova, V.V. and Shchegolikhin, A., 2008. Effect of the content of ethyl cellulose-rubber blend on physicochemical properties of adhesive compositions. *Article in Polymer Science Series D*. [online] https://doi.org/10.1134/S1995421208030040.

Nag, A., Mitra, A. and Mukhopadhyay, S.C., 2018. Graphene and its sensor-based applications: A review. *Sensors and Actuators A: Physical*, 270, pp.177–194. https://doi.org/10.1016/J.SNA.2017.12.028.

Nag, A., Simorangkir, R.B.V.B., Gawade, D.R., Nuthalapati, S., Buckley, J.L., O'Flynn, B., Altinsoy, M.E. and Mukhopadhyay, S.C., 2022. *Graphene-based wearable temperature sensors: A review*. *Materials and Design*, https://doi.org/10.1016/j.matdes.2022.110971.

Naik, G. and Krishnaswamy, S., 2016. Room-Temperature Humidity Sensing Using Graphene Oxide Thin Films. *Graphene*, [online] 05(01), pp.1–13. https://doi.org/10.4236/GRAPHENE.2016.51001.

Nishino, T., Matsuda, I. and Hirao, K., 2004. All-Cellulose Composite. *Macromolecules*, [online] 37(20), pp.7683–7687. https://doi.org/10.1021/MA049300H.

Nishiyama, Y., Sugiyama, J., Chanzy, H. and Langan, P., 2003. Crystal Structure and Hydrogen Bonding System in Cellulose Iα from Synchrotron X-

ray and Neutron Fiber Diffraction. *Journal of the American Chemical Society*, 125(47), pp.14300–14306. https://doi.org/10.1021/JA037055W.

Noreen, A., Zia, K.M., Tabasum, S., Khalid, S. and Shareef, R., 2020. A review on grafting of hydroxyethylcellulose for versatile applications. *International Journal of Biological Macromolecules*, 150, pp.289–303. https://doi.org/10.1016/J.IJBIOMAC.2020.01.265.

Novoselov, K.S., Fal'Ko, V.I., Colombo, L., Gellert, P.R., Schwab, M.G. and Kim, K., 2012. A roadmap for graphene. *Nature 2012 490:7419*, [online] 490(7419), pp.192–200. https://doi.org/10.1038/nature11458.

Ojha, K., Anjaneyulu, O. and Ganguli, A.K., 2014. Graphene-based hybrid materials: synthetic approaches and properties. *CARBON TECHNOLOGY CURRENT SCIENCE*, 107(3).

Ouarga, A., Noukrati, H., Iraola-Arregui, I., Elaissari, A., Barroug, A. and Ben youcef, H., 2020. Development of anti-corrosion coating based on phosphorylated ethyl cellulose microcapsules. *Progress in Organic Coatings*, 148, p.105885. https://doi.org/10.1016/J.PORGCOAT.2020.105885.

Pech, D., Brunet, M., Durou, H., Huang, P., Mochalin, V., Gogotsi, Y., Taberna, P.L. and Simon, P., 2010. Ultrahigh-power micrometre-sized supercapacitors based on onion-like carbon. *Nature Nanotechnology 2010 5:9*, [online] 5(9), pp.651–654. https://doi.org/10.1038/nnano.2010.162.

Pop, E., Varshney, V. and Roy, A.K., 2012. Thermal properties of graphene: Fundamentals and applications. *MRS Bulletin*, [online] 37(12), pp.1273–1281. https://doi.org/10.1557/MRS.2012.203.

Popov, V.I., Nikolaev, D. V., Timofeev, V.B., Smagulova, S.A. and Antonova, I. V., 2017. Graphene-based humidity sensors: the origin of alternating resistance change. *Nanotechnology*, [online] 28(35), p.355501. https://doi.org/10.1088/1361-6528/AA7B6E.

Qi, X., Li, X., Jo, H., Sideeq Bhat, K., Kim, S., An, J., Kang, J.W. and Lim, S., 2020. Mulberry paper-based graphene strain sensor for wearable electronics with high mechanical strength. *Sensors and Actuators A: Physical*, 301, p.111697. https://doi.org/10.1016/J.SNA.2019.111697.

Quellmalz, A., Smith, A.D., Elgammal, K., Fan, X., Delin, A., Östling, M., Lemme, M., Gylfason, K.B. and Niklaus, F., 2018. Influence of Humidity on Contact Resistance in Graphene Devices. *ACS Applied Materials and Interfaces*, [online] 10(48), pp.41738–41746. https://doi.org/10.1021/ACSAMI.8B10033/ASSET/IMAGES/MEDIUM/AM-2018-100332_M008.GIF.

Raval, S., 2018. Ultrafast Pump-Probe spectroscopy of Graphene Oxide (GO) and Reduced Graphene Oxide (RGO). [online] https://doi.org/10.13140/RG.2.2.13862.57923.

Richards, H.L., Baker, P.G.L. and Iwuoha, E., 2012. Metal Nanoparticle Modified Polysulfone Membranes for Use in Wastewater Treatment: A Critical Review. *Journal of Surface Engineered Materials and Advanced Technology*, 02(03), pp.183–193. https://doi.org/10.4236/jsemat.2012.223029.

Sadasivuni, K.K., Kafy, A., Kim, H.C., Ko, H.U., Mun, S. and Kim, J., 2015. Reduced graphene oxide filled cellulose films for flexible temperature sensor application. *Synthetic Metals*, 206, pp.154–161. https://doi.org/10.1016/J.SYNTHMET.2015.05.018.

Sahatiya, P., Puttapati, S.K., Srikanth, V.V.S.S. and Badhulika, S., 2016. Graphene-based wearable temperature sensor and infrared photodetector on a flexible polyimide substrate. *Flexible and Printed Electronics*, [online] 1(2), p.025006. https://doi.org/10.1088/2058-8585/1/2/025006.

Sara, S.M., Al-Dhahebi, A.M. and Mohamed Saheed, M.S., 2022. Recent Advances in Graphene-Based Nanocomposites for Ammonia Detection. *Polymers*, [online] 14(23). https://doi.org/10.3390/POLYM14235125.

Seddiqi, H., Oliaei, E., Honarkar, H., Jin, J., Geonzon, L.C., Bacabac, R.G. and Klein-Nulend, J., 2021. Cellulose and its derivatives: towards biomedical applications. *Cellulose 2021 28:4*, [online] 28(4), pp.1893–1931. https://doi.org/10.1007/S10570-020-03674-W.

Seekaew, Y., Lokavee, S., Phokharatkul, D., Wisitsoraat, A., Kerdcharoen, T. and Wongchoosuk, C., 2014. Low-cost and flexible printed graphene–PEDOT:PSS gas sensor for ammonia detection. *Organic Electronics*, 15(11), pp.2971–2981. https://doi.org/10.1016/J.ORGEL.2014.08.044.

Segev-Bar, M., Bachar, N., Wolf, Y., Ukrainsky, B., Sarraf, L. and Haick, H., 2017. Multi-Parametric Sensing Platforms Based on Nanoparticles. *Advanced Materials Technologies*, [online] 2(1), p.1600206. https://doi.org/10.1002/ADMT.201600206.

Shahil, K.M.F. and Balandin, A.A., 2012. Thermal properties of graphene and multilayer graphene: Applications in thermal interface materials. *Solid State Communications*, 152(15), pp.1331–1340. https://doi.org/10.1016/J.SSC.2012.04.034.

Singh, E., Meyyappan, M. and Nalwa, H.S., 2017. Flexible Graphene-Based Wearable Gas and Chemical Sensors. *ACS Applied Materials and Interfaces*, [online] 9(40), pp.34544–34586. https://doi.org/10.1021/ACSAMI.7B07063/ASSET/IMAGES/MEDIUM/AM-2017-070638_0033.GIF.

Spyrou, K. and Rudolf, P., 2014. An Introduction to Graphene. *Functionalization of Graphene*, [online] 9783527335510, pp.1–20. https://doi.org/10.1002/9783527672790.CH1.

Trung, T.Q. and Lee, N.E., 2016. Flexible and Stretchable Physical Sensor Integrated Platforms for Wearable Human-Activity Monitoringand Personal

Healthcare. *Advanced Materials*, [online] 28(22), pp.4338–4372. https://doi.org/10.1002/ADMA.201504244.

Vilela, D., Romeo, A. and Sánchez, S., 2016. Flexible sensors for biomedical technology. *Lab on a Chip*, [online] 16(3), pp.402–408. https://doi.org/10.1039/C5LC90136G.

Wasilewska, K. and Winnicka, K., 2019. Ethylcellulose–A Pharmaceutical Excipient with Multidirectional Application in Drug Dosage Forms Development. *Materials 2019, Vol. 12, Page 3386*, [online] 12(20), p.3386. https://doi.org/10.3390/MA12203386.

Xie, J., Chen, Q., Shen, H. and Li, G., 2020. Review—Wearable Graphene Devices for Sensing. *Journal of The Electrochemical Society*, [online] 167(3), p.037541. https://doi.org/10.1149/1945-7111/AB67A4.

Yan, Z., Nika, D.L. and Balandin, A.A., 2015. Thermal properties of graphene and few-layer graphene: applications in electronics. *IET Circuits, Devices & Systems*, [online] 9(1), pp.4–12. https://doi.org/10.1049/IET-CDS.2014.0093.

Yang, G., Li, L., Lee, W.B. and Ng, M.C., 2018. Structure of graphene and its disorders: a review. *http://www.tandfonline.com/action/journalInformation?show=aimsScope&journalCode=tsta20#.VmBmuzZFCUk*, [online] 19(1), pp.613–648. https://doi.org/10.1080/14686996.2018.1494493.

Yao, Y., Chen, X., Zhu, J., Zeng, B., Wu, Z. and Li, X., 2012. The effect of ambient humidity on the electrical properties of graphene oxide films. *Nanoscale Research Letters*, 7, pp.2–19. https://doi.org/10.1186/1556-276X-7-363.

Yin, F., Ye, D., Zhu, C., Qiu, L. and Huang, Y.A., 2017. Stretchable, Highly Durable Ternary Nanocomposite Strain Sensor for Structural Health Monitoring of Flexible Aircraft. *Sensors 2017, Vol. 17, Page 2677*, [online] 17(11), p.2677. https://doi.org/10.3390/S17112677.

Yin, Z., Zhu, J., He, Q., Cao, X., Tan, C., Chen, H., Yan, Q. and Zhang, H., 2014. Graphene-Based materials for solar cell applications. *Advanced Energy Materials*, 4(1). https://doi.org/10.1002/AENM.201300574.

Yoshida, A., Wang, Y.F., Tachibana, S., Hasegawa, A., Sekine, T., Takeda, Y., Hong, J., Kumaki, D., Shiba, T. and Tokito, S., 2022. Printed, all-carbon-based flexible humidity sensor using a cellulose nanofiber/graphene nanoplatelet composite. *Carbon Trends*, 7, p.100166. https://doi.org/10.1016/J.CARTRE.2022.100166.

Yu, K., Wang, P., Lu, G., Chen, K.H., Bo, Z. and Chen, J., 2011. Patterning vertically oriented graphene sheets for nanodevice applications. *Journal of Physical Chemistry Letters*, [online] 2(6), pp.537–542. https://doi.org/10.1021/JZ200087W/SUPPL_FILE/JZ200087W_SI_001.PDF.

Zhang, Y.H.P. and Lynd, L.R., 2004. Toward an aggregated understanding of enzymatic hydrolysis of cellulose: Noncomplexed cellulase systems. *Biotechnology and Bioengineering*, [online] 88(7), pp.797–824. https://doi.org/10.1002/BIT.20282.

Zhang, Z. and Yang, R., 2017. Novel nanocomposites based on hydroxyethyl cellulose and graphene oxide. *Fibers and Polymers*, [online] 18(2), pp.334–341. https://doi.org/10.1007/S12221-017-6901-9/METRICS.

Zhong, Y.L., Tian, Z., Simon, G.P. and Li, D., 2015. Scalable production of graphene via wet chemistry: progress and challenges. *Materials Today*, 18(2), pp.73–78. https://doi.org/10.1016/J.MATTOD.2014.08.019.

Zulkifli, F.H., Hussain, F.S.J., Rasad, M.S.B.A. and Mohd Yusoff, M., 2014. Nanostructured materials from hydroxyethyl cellulose for skin tissue engineering. *Carbohydrate Polymers*, 114, pp.238–245. https://doi.org/10.1016/J.CARBPOL.2014.08.019.

APPENDICES

Appendix A: Figures

Figure A – 1:   (left to right) Prototypes used in ammonia-sensing test, temperature-sensing test, bending test, and human respiration monitoring test.
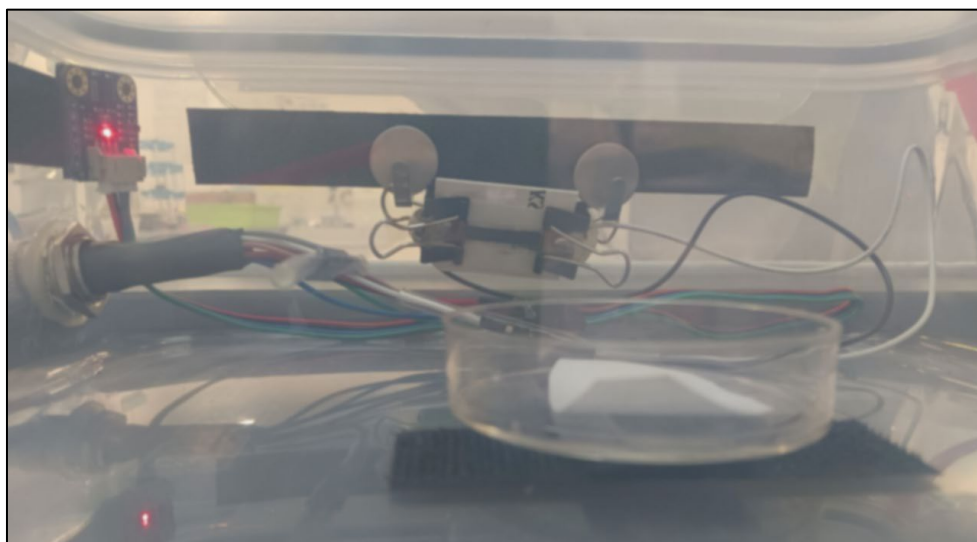

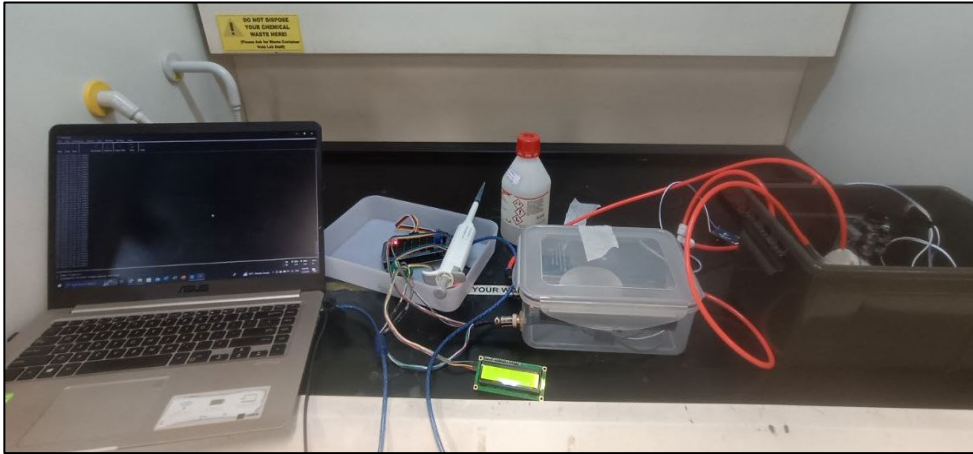Figure A – 2:   Setup of ammonia-sensing test.

Figure A – 3:   Setup of gas pump, gas chamber and data acquisition for ammonia-sensing test.
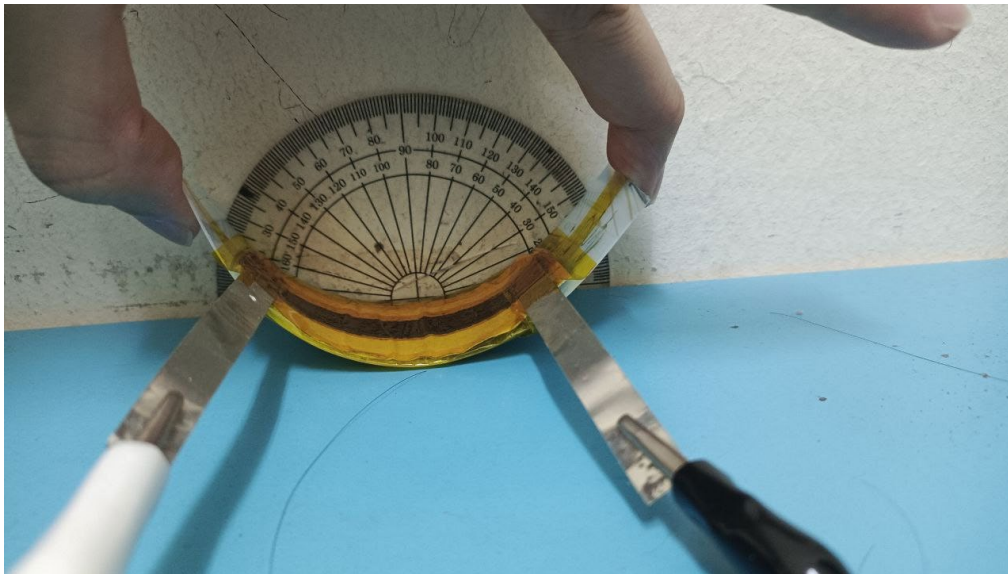

Figure A – 4:   Testing of bending performance.

```
const int sensorPin = A1; // Pin for the voltage divider

int r2 = 100 // kOhms, value of fixed resistor

void setup () {
  Serial.begin (9600); // start serial communication
}

void loop () {
  sensorValue = analogRead(sensorPin); // read the analog in bit
  float voltage = (sensorValue / 1023.0000) * 5.0000; // convert the analog value to voltage, preserving 4 d.c.
  float r1 = voltage * r2 / (5.0000 = voltage); // in kOhm
  Serial.println(r1); // Print the measured resistance to the serial monitor
  delay(60); // 60 ms time interval for a data
}
```

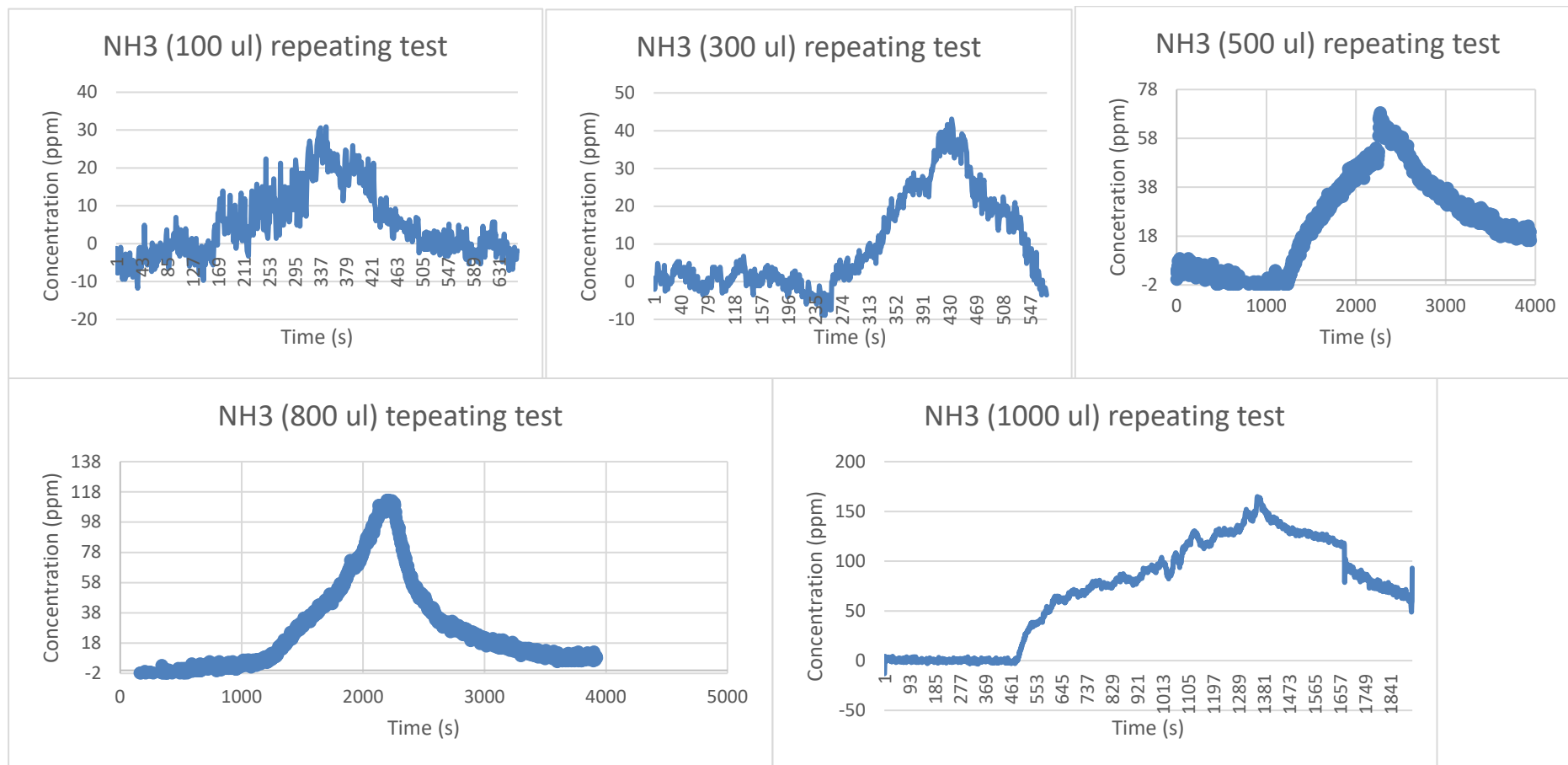Figure A – 5:   Source code of Arduino voltage-divider as data acquisition.

Figure A – 6:   Data collection from repeating test of ammonia-sensing modal using linear regression model.

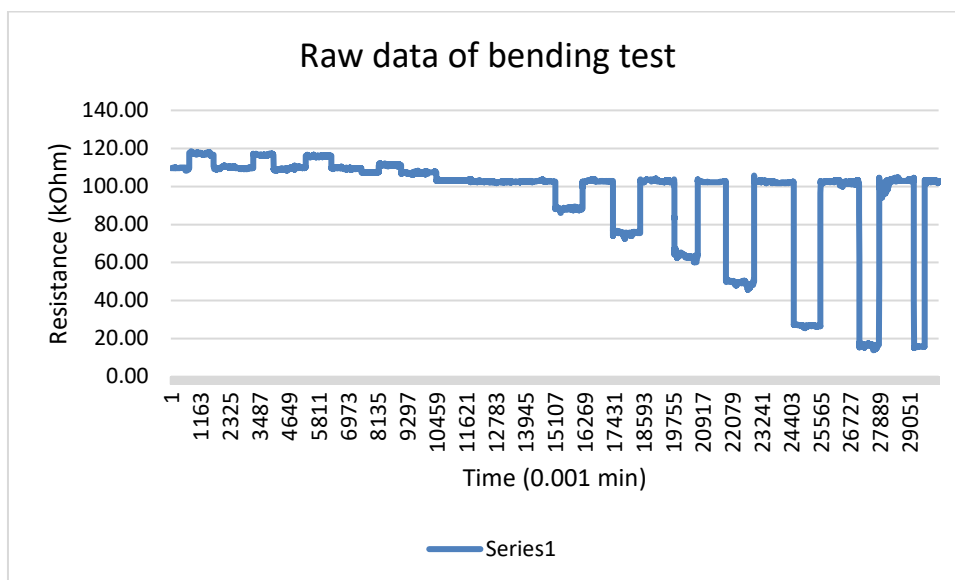Figure A – 7:   Data collection from bending test.

Figure A – 8: 5th order polynomial equation for general bending response.
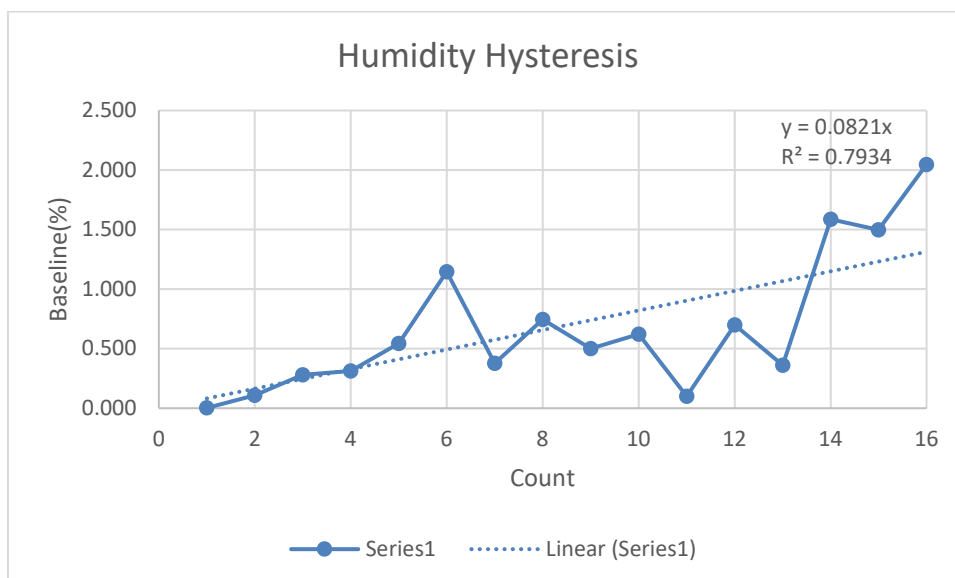

Figure A – 9:   Linear variation of baseline resistance to number of exhalation (starting from initialization, no exhalation).

Appendix B: Tables

Table B – 1:   Thickness of GNP/HEC sensing layer by random sampling.

Count	Angle (degree)	Thickness (um)
1	90.000	23.345
2	90.000	21.080
3	90.000	12.718
4	90.000	21.429
5	90.000	23.693
6	90.000	11.672
7	90.000	29.024
8	90.000	27.178
9	90.000	23.693
10	90.387	25.785
11	90.000	28.746
12	90.000	22.997
13	90.000	26.777
14	89.469	28.224
15	90.000	20.383
16	90.000	35.017
17	90.000	23.780
18	90.000	20.383
19	90.000	27.700
20	90.000	35.017
21	90.000	14.373
22	90.651	22.998
23	90.000	28.084
24	90.000	24.948
25	90.000	33.449
26	90.000	36.063
27	90.000	20.906
28	90.000	26.132
29	90.000	28.746
30	90.000	28.223
31	90.000	32.666
32	90.000	15.941
33	90.000	37.108
34	90.000	31.812
35	90.000	29.268
36	90.000	19.861
37	90.000	20.906
38	90.000	22.474
39	90.000	9.930
40	90.000	22.474
41	90.000	17.770

42	90.000	16.725
43	90.000	30.314
44	90.000	24.390
45	90.000	19.338
46	90.000	29.268
47	90.000	37.108
48	90.000	30.314
49	90.000	18.815
50	90.000	20.906
Mean	**90.010**	**24.799**
SD	**0.132**	**6.536**
Min	**89.469**	**9.930**
Max	**90.651**	**37.108**

Table B – 2: Sheet resistance of a bare GNP/HEC sensitive at 14 different locations measured by using four-point probe.

Probing location	Mean Sheet Resistance (Ohm/sq)	Mean Resistivity (Ohm.m)	Mean Conductivity (S/m)
Center 1	7263.20499	0.18013	5.55180
Center 2	9276.57629	0.23006	4.34678
Center 3	3743.86785	0.09285	10.77031
Center 4	4587.06531	0.11376	8.79051
Center 5	4377.54047	0.10856	9.21134
Center 6	5765.68462	0.14299	6.99357
Right 1	6335.13178	0.15711	6.36494
Right 2	7796.57712	0.19336	5.17187
Right 3	9056.02667	0.22459	4.45257
Right 4	4488.34316	0.11131	8.98388
Left 1	3344.04307	0.08293	12.05806
Left 2	4748.09746	0.11775	8.49238
Left 3	3414.56337	0.08468	11.80902
Left 4	3568.80919	0.08851	11.29872
Mean	**5554.68081**	**0.13776**	**8.16398**
SD	**2066.39881**	**0.05125**	**2.71842**
Min	**3344.04307**	**0.08293**	**4.34678**
Max	**9276.57629**	**0.23006**	**12.05806**